The Astrophysical Journal, 989:156 (19pp), 2025 August 20 https://doi.org/10.3847/1538-4357/aded90

Cold Gas and Star Formation in the Phoenix Cluster with JWST

Michael Reefe[1,18], Michael McDonald[1], Marios Chatzikos[2], Jerome Seebeck[3], Richard Mushotzky[3], Sylvain Veilleux[3], Steven W. Allen[4,5,6], Matthew Bayliss[7], Michael Calzadilla[8], Rebecca Canning[9], Megan Donahue[10], Benjamin Floyd[9,11], Massimo Gaspari[12], Julie Hlavacek-Larrondo[13], Brian McNamara[14], Helen Russell[15], Arnab Sarkar[1], Keren Sharon[16], and Taweewat Somboonpanyakul[17]
[1] Kavli Institute for Astrophysics & Space Research, Massachusetts Institute of Technology, Cambridge, MA 02139, USA; mreefe@mit.edu
[2] Department of Physics & Astronomy, University of Kentucky, Lexington, KY 40506, USA
[3] Department of Astronomy & Joint Space-Science Institute, University of Maryland, College Park, College Park, MD 20740, USA
[4] Kavli Institute for Particle Astrophysics and Cosmology, Stanford University, 452 Lomita Mall, Stanford, CA 94305, USA
[5] Department of Physics, Stanford University, 382 Via Pueblo Mall, Stanford, CA 94305, USA
[6] SLAC National Accelerator Laboratory, 2575 Sand Hill Road, Menlo Park, CA 94025, USA
[7] Department of Physics, University of Cincinnati, Cincinnati, OH 45221, USA
[8] Center for Astrophysics, Harvard & Smithsonian, 60 Garden Street, Cambridge, MA 02138, USA
[9] Institute of Cosmology & Gravitation, University of Portsmouth, Dennis Sciama Building, Portsmouth, PO1 3FX, UK
[10] Department of Physics and Astronomy, Michigan State University, East Lansing, MI 48824, USA
[11] Department of Physics and Astronomy, University of Missouri-Kansas City, Flarsheim Hall, 5110 Rockhill Road, Kansas City, MO 64110, USA
[12] Department of Physics, Informatics and Mathematics, University of Modena and Reggio Emilia, 41125 Modena, Italy
[13] Department of Physics, Université de Montréal, Montreal, QC H3T 1J4, Canada
[14] Department of Physics and Astronomy, University of Waterloo, Waterloo, ON N2L 3G1, Canada
[15] School of Physics & Astronomy, University of Nottingham, University Park, Nottingham NG7 2RD, UK
[16] Department of Astronomy, University of Michigan, 1085 S. University Avenue, Ann Arbor, MI 48109, USA
[17] Department of Physics, Faculty of Science, Chulalongkorn University, 254 Phayathai Road, Pathumwan, Bangkok 10330, Thailand
Received 2025 January 14; revised 2025 June 12; accepted 2025 July 7; published 2025 August 12

Abstract

We present integral field unit observations of the Phoenix Cluster with the JWST Mid-infrared Instrument's Medium Resolution Spectrometer. We focus this study on the molecular gas, dust, and star formation in the brightest cluster galaxy (BCG). We use precise spectral modeling to produce maps of the silicate dust, molecular gas, and polycyclic aromatic hydrocarbons (PAHs) in the inner ∼50 kpc of the cluster. We measure the optical depth from silicates by comparing the observed H_2 line ratios to those predicted by excitation models. We provide updated measurements of the total molecular gas mass of $1.9^{+0.5}_{-0.4} \times 10^{10}\,M_\odot$, which agrees with CO-based estimates, providing an estimate of the CO-to-H_2 conversion factor of $\alpha_{CO} = 0.8 \pm 0.2\ M_\odot\ pc^{-2}\ (K\ km\ s^{-1})^{-1}$; an updated stellar mass of $M_* = 2.6 \pm 0.5 \times 10^{10}\,M_\odot$; and star formation rates (SFRs) averaged over 10 and 100 Myr of $\langle SFR \rangle_{10} = 1340 \pm 100\,M_\odot\,yr^{-1}$ and $\langle SFR \rangle_{100} = 740 \pm 80\,M_\odot\,yr^{-1}$, respectively. The H_2 emission seems to be powered predominantly by shocks and star formation within the central ∼20 kpc, induced by stellar feedback and radio jets from the active galactic nucleus. Additionally, we find nearly an order-of-magnitude drop in the SFRs estimated by PAH fluxes in cool core BCGs compared to field galaxies, suggesting that hot particles from the intracluster medium are destroying PAH grains even in the central-most tens of kiloparsecs.

Unified Astronomy Thesaurus concepts: Galaxy clusters (584); Infrared astronomy (786); Cooling flows (2028); Active galaxies (17); Elliptical galaxies (456); Starburst galaxies (1570); Intracluster medium (858); Interstellar dust extinction (837)

1. Introduction

The hot intracluster medium (ICM) that permeates clusters of galaxies exists at temperatures of the order of 10^7 K and emits thermal bremsstrahlung radiation in the X-ray. This radiation causes it to lose energy and cool down over time. Once the gas cools to $\sim 10^{6.5}$ K, it will start to radiate through other mechanisms, primarily metal line emission, increasing the rate of cooling. Individual ionization states of metal species will contribute to the cooling at different temperatures, determined by the temperatures at which their collisional ionization equilibrium abundances are maximized. The many complex physical processes that contribute to the cooling rate of the gas at different temperatures are commonly conglomerated into a single entity called the cooling function $\Lambda(T)$ (i.e., R. S. Sutherland & M. A. Dopita 1993). This, in combination with the initial thermal energy (per unit volume) of the gas $\mathcal{E}$, can give an idea of the overall cooling time, $t_{cool} \sim \mathcal{E}/n^2\Lambda \propto T^{1/2}n^{-1}$. If the initial temperature of the gas is not too high, and its density is not too low, then a cooling flow may develop within cooling times less than the age of the Universe, meaning they should be observable (A. C. Fabian et al. 1984). In the classical (isobaric) picture, a cooling flow unfolds as follows (see, e.g., H. Mo et al. 2010). Consider a parcel of ICM gas that cools by an incremental amount—its temperature drops, and by the ideal gas law so does its pressure. The weight of the surrounding gas now pushes on the parcel, causing it to move inward and increase in density. The change in density causes a corresponding change in pressure until it can again reach a state of equilibrium with the surrounding gas.

[18] National Science Foundation, Graduate Research Fellow.

These cooling flow models provide compelling explanations for the presence and origin of 10^5–10^6 K ionized gas in the interstellar, circumgalactic, intragroup, and intracluster media (R. Bordoloi et al. 2017). However, ideal cooling flows like described above cannot exist in nature because cooling can never be 100% efficient. Heating, turbulence, and magnetic fields are just a few examples of physical processes that reduce cooling efficiency and prevent unabated cooling flows from developing. Indeed, if the gas were able to cool unabated from the hot $\sim 10^7$ K atmosphere to the cold 10 K molecular phase and rapidly form stars, we should observe star formation rates (SFRs) in brightest cluster galaxies (BCGs) of a similar magnitude to the classical cooling rates measured from the ICM. In reality, the observed SFRs are typically suppressed by 2 orders of magnitude relative to the cooling rates (B. R. McNamara & R. W. O'Connell 1989; S. W. Allen 1995; C. S. Crawford et al. 1999; A. K. Hicks & R. Mushotzky 2005; L. O. V. Edwards et al. 2007; N. A. Hatch et al. 2007; C. P. O'Dea et al. 2008; M. McDonald et al. 2010, 2018; A. S. Hoffer et al. 2012; T. D. Rawle et al. 2012; M. Donahue et al. 2015; R. Mittal et al. 2015; S. Molendi et al. 2016; M. S. Calzadilla et al. 2023). Studying the cold gas content and stellar populations in galaxy clusters is, therefore, crucial for understanding the end stages of these cooling flows, which illuminates how they affect the evolution of BCGs.

Cooling flows are expected to last for a significant fraction of a cluster's lifetime based on the incidence rate of cool core clusters in the general galaxy cluster population. For timescales of Gyr, the amount of molecular gas formed should be on the order 10^{11}–$10^{12}\,M_\odot$. Nevertheless, observed molecular gas masses consistently fall short of this prediction, typically ranging from 10^8–$10^{10}\,M_\odot$ (A. C. Edge 2001; P. Salomé & F. Combes 2003; P. Salomé et al. 2008). This, in conjunction with the low SFRs, is evidence that a large fraction of the gas is not able to fully cool and is being reheated, likely by feedback from an active galactic nucleus (AGN) in the core (see reviews by B. R. McNamara & P. E. J. Nulsen 2007; A. C. Fabian 2012; M. Gaspari et al. 2020). Thus, the classical steady isobaric picture of cooling flows is most likely not an accurate representation of how cooling actually takes place in these clusters. Simulations and theories now suggest that cooling proceeds as a more chaotic, turbulent cascade of condensing cold clouds that periodically precipitate onto and fuel accretion (feeding) and feedback episodes of the central supermassive black hole (SMBH; M. Gaspari et al. 2011, 2018; D. Prasad et al. 2015; Y. Li et al. 2017).

Dust content is also important to consider in the context of cooling flows—dust grains are closely linked with the cold molecular gas, acting as "seeds" for the gas to clump into star-forming regions and filaments, boosting condensation and the cooling cascade and enriching the stellar populations. The presence of dust can inform the presence of cold gas and stars, and vice versa (F. Calura et al. 2008; S. Kaviraj et al. 2012). It is especially important when considering attenuation effects, which are dependent on both wavelength and geometry and can complicate measurements of the cooling rates and inferences made from these measurements. Cooling rates measured from emission lines in the UV, such as O VI$\lambda\lambda$1032,1038 Å, can be significantly underestimated if an extinction correction is not taken into account. Absorption effects may also partially explain why many lines in the soft X-ray regime below $10^{6.5}$ K seem to be absent or much weaker than expected in many systems (C. R. Canizares et al. 1988; L. P. David et al. 2001; J. R. Peterson et al. 2003), implying much of the cooling gas is "hidden," but may still be fueling massive cooling flows down to the molecular gas regime (A. C. Fabian et al. 2022, 2023).

The Phoenix Cluster (SPT-CLJ2344-4243; R. Williamson et al. 2011; M. McDonald et al. 2012) is an interesting case study in the field of cooling flows. Its extreme 500–800 $M_\odot\,\mathrm{yr}^{-1}$ starburst represents $\sim$10%–20% of the 3800 $M_\odot\,\mathrm{yr}^{-1}$ classical cooling rate (compared to the typical 1%; M. McDonald et al. 2012), and it contains a massive $2.1 \pm 0.3 \times 10^{10}\,M_\odot$ reservoir of cold molecular gas (H. R. Russell et al. 2017), both signs which point to it being one of the most rapid and uninhibited cooling flows in the known Universe. This makes it an ideal playground to study the effects of large-scale cooling on host galaxies. However, due to the complex nature of this system, which hosts an extremely luminous type II QSO on top of a massive cooling flow, many of these measurements are marred by systematic uncertainties relating to how much of the underlying emission can be attributed to the QSO, how much dust extinction there is, and the metallicity of the ICM. The molecular gas mass estimate in particular relies on an uncertain conversion factor between CO and H_2, α_{CO}, which may vary by a factor of a few depending on the density, temperature, and metallicity of the molecular clouds (A. D. Bolatto et al. 2013).

Our recent work (M. Reefe et al. 2025, hereafter R25) looked at this unique cluster through an infrared lens with observations using JWST's Mid-infrared Instrument in Medium Resolution Spectroscopy mode (MIRI/MRS), which has the advantage of being in a wavelength regime with essentially no extinction. R25 focused on the intermediate-temperature ($10^{5.5}$ K) coronal gas, using the high-ionization [Ne VI] , [Ne v] , [Fe VIII], [Fe VII], and [Mg VII] lines to reveal the morphology, kinematics, and cooling rate of the gas in between the hot and cold phases. In this work, we wish to examine this same data set through a new lens, now with a focus on the molecular gas, dust, and star formation. The mid-infrared spectral range covered by MIRI/MRS is rich in spectral features from warm molecular gas (the rotational H_2 emission lines), dust (the thermal dust continuum and the 9.7 μm silicate absorption feature), and very small dust grains known as polycyclic aromatic hydrocarbons (PAHs; which exhibit broad emission features). We have four primary goals with this analysis, which we tackle in sequence throughout this paper: (1) Understand the morphology of the warm molecular gas, dust, and PAHs and how they relate to heating and feedback sources (i.e., radio jets) and the other gas phases, most notably the cold molecular gas seen in CO; (2) obtain an independent measurement of the total molecular gas mass directly from the H_2 emission lines, without relying on the uncertain α_{CO} conversion factor; (3) use this new data to get better constraints on the star formation history, and a more precise measurement of the current SFR; and (4) use correlations and known scaling relations between IR spectral features to obtain constraints on the importance of different heating mechanisms in exciting the molecular gas and dust, and compare these with the typical cool core BCG population.

To aid with our fourth goal, we build upon the work of M. Donahue et al. (2011), hereafter D11, who studied a sample of cool core (CC) BCGs using infrared spectra and photometry from the Spitzer Space Telescope. Correlations between the

emission features from dust, PAHs, molecular gas, and warm ionized gas are often seen in galaxies of different types and can give insights into the dominant physical mechanisms that power the emission. Gas and dust can be heated through star formation, cosmic rays, suprathermal ICM electrons, photoelectrons ejected from dust grains, shocks, and/or AGN feedback in the form of mechanical radio jets, radiative winds, and turbulence (M. Gaspari et al. 2011; J. Hlavacek-Larrondo et al. 2015; D. Prasad et al. 2015). D11 found a number of such correlations in the CC BCG population using spectral features in the mid-infrared (MIR), and the Infrared Spectrograph on Spitzer covers a very similar spectral range as MIRI/MRS, so we find these correlations useful as a comparison point for the Phoenix Cluster.

This paper is organized as follows. The observations and data reduction methods are presented in Section 2. Then, Section 3 goes over our analysis of the gas and dust morphology (Section 3.1) and the stellar populations (Section 3.2). Section 4 then goes into the correlation analysis, discussing and interpreting our findings in the context of the global picture of the cooling flow and the theory that Phoenix may contain an undermassive SMBH. We then summarize our findings in Section 5. Throughout this work, we assume a flat Λ cold dark matter cosmology with $\Omega_m = 0.27$, $\Omega_\Lambda = 0.73$, and $H_0 = 70$ km s^{-1} Mpc^{-1}.

2. Observations

2.1. Data Collection

We obtained JWST MIRI/MRS observations of the Phoenix Cluster on UTC 2023 July 27–28 with program ID 2439. Exposures were taken in all channel/band combinations. The SHORT (A) band exposures were the longest, at 6.95 hr (since the primary science goal of this program was measuring the [Ne VI] emission, i.e., R25), while the MEDIUM (B) and LONG (C) band exposures were 51.0 and 85.8 minutes, respectively. Dedicated background exposures were also taken, with exposure times of 51.0, 16.8, and 25.2 minutes. On-source exposures used a four-point dither pattern, while background exposures used a two-point dither pattern. In the rest frame of Phoenix A ($z = 0.597$), MIRI/MRS covers a wavelength range of 3.1–17.5 μm.

2.2. Data Reduction

Here, we provide a brief overview of the general steps taken in the data reduction, cleaning, and correction processes. For full details on these procedures, see R25. We use the STScI pipeline version 1.12.3 and CRDS context `jwst_1140.pmap` to reduce the MIRI/MRS data. We use a few nonstandard settings, including more aggressive cosmic-ray flagging (lowering the jump rejection threshold to 3.5σ and enabling cosmic-ray shower flagging[19]), 2D residual fringe correction (removing fixed-frequency modulations in the spectrum caused by standing waves[20]), and 2D pixel-by-pixel background subtraction.[21] We also perform a few additional data cleaning procedures. We remove hot/warm pixels by flagging outliers in the background exposures and masking them in both the background and science frames, following J. S. Spilker et al. (2023). The thresholds for flagging outliers were chosen by hand for each channel and tried to keep a balance between keeping as much data as possible and making sure to exclude obviously bad pixels. The (low, high) threshold pixel values for channels 1 and 2, 3, and 4, after subtracting the median, were (−0.14, + 0.13), (−0.16, +0.10), and (−0.16, +0.27), respectively. We also remove stripe artifacts caused by cosmic-ray hits, also following J. S. Spilker et al. (2023). Additionally, we rescale the data to account for the loss in sensitivity over time of MIRI. This effect has been accounted for in the 1.12.3 version of the STSci pipeline, but we have found that the corrected fluxes still underpredict independently measured infrared fluxes from the Wide-field Infrared Survey Explorer (WISE). We therefore take the wavelength-dependent correction vector from the STSci pipeline and rescale it until the data match the observed WISE fluxes within 1σ. We also replace the pipeline-produced errors with our own estimates of the pixel-by-pixel scatter by measuring the rms variation between the data and a cubic spline fit with a spacing of 7 pixels between knots (masking emission lines).

Our data has a bright point source due to the IR-bright QSO at the center of Phoenix A. We are, therefore, interested in modeling the point-spread function (PSF) of MIRI/MRS. To do so, we use data of the bright star 16 Cygni B from program ID 1538. We shift the centroid of the star to match the position of our Phoenix A data, normalize such that it integrates to 1 at each wavelength slice, and fit a cubic spline along the wavelength axis with 100 pixels between each knot. The normalization is done to remove the spectral shape of the star, and the spline fitting is done to reduce the noise in the extracted PSF profile, which should only vary gradually with wavelength. Again, for full details on these procedures, refer to R25. Figure 1 shows an example of a bright off-nuclear spectrum and model.

3. Results

3.1. Gas and Dust Content

We use the Likelihood Optimization of gas Kinematics in Integral Field Units (LOKI; M. Reefe 2025)[22] code to perform least-squares fits of the spectra in each spaxel. During the fitting procedure, the light from each spaxel is separated into a host galaxy component and a QSO component. The former traces the underlying emission from the gas, dust, and stars within and along the line of sight (LOS) of the BCG at the location of the spaxel. The latter traces light from the central QSO that has been dispersed according to the PSF and contaminates the observed spectrum of the spaxel. For these fits, we follow the methods of R25.

3.1.1. Silicate Dust Obscuration

We first perform a set of initial fits for each individual channel. In these initial fits, the recovered optical depth τ of the host galaxy is unreliable because the QSO spectrum outshines the host galaxy within ∼15 kpc of the center (due to the PSF). The faint continuum of the host galaxy becomes dominated by instrumental systematics that make it difficult to measure τ from the shape of the silicate absorption feature. As such, we measure the optical depth of the host galaxy using an independent method that only relies on the flux ratios of the rotational H_2 lines obtained from these initial fits. In contrast to

[19] JWST pipeline cosmic ray snowball/shower information
[20] JWST Pipeline fringing information
[21] JWST pipeline background subtraction information
[22] https://github.com/Michael-Reefe/Loki.jl

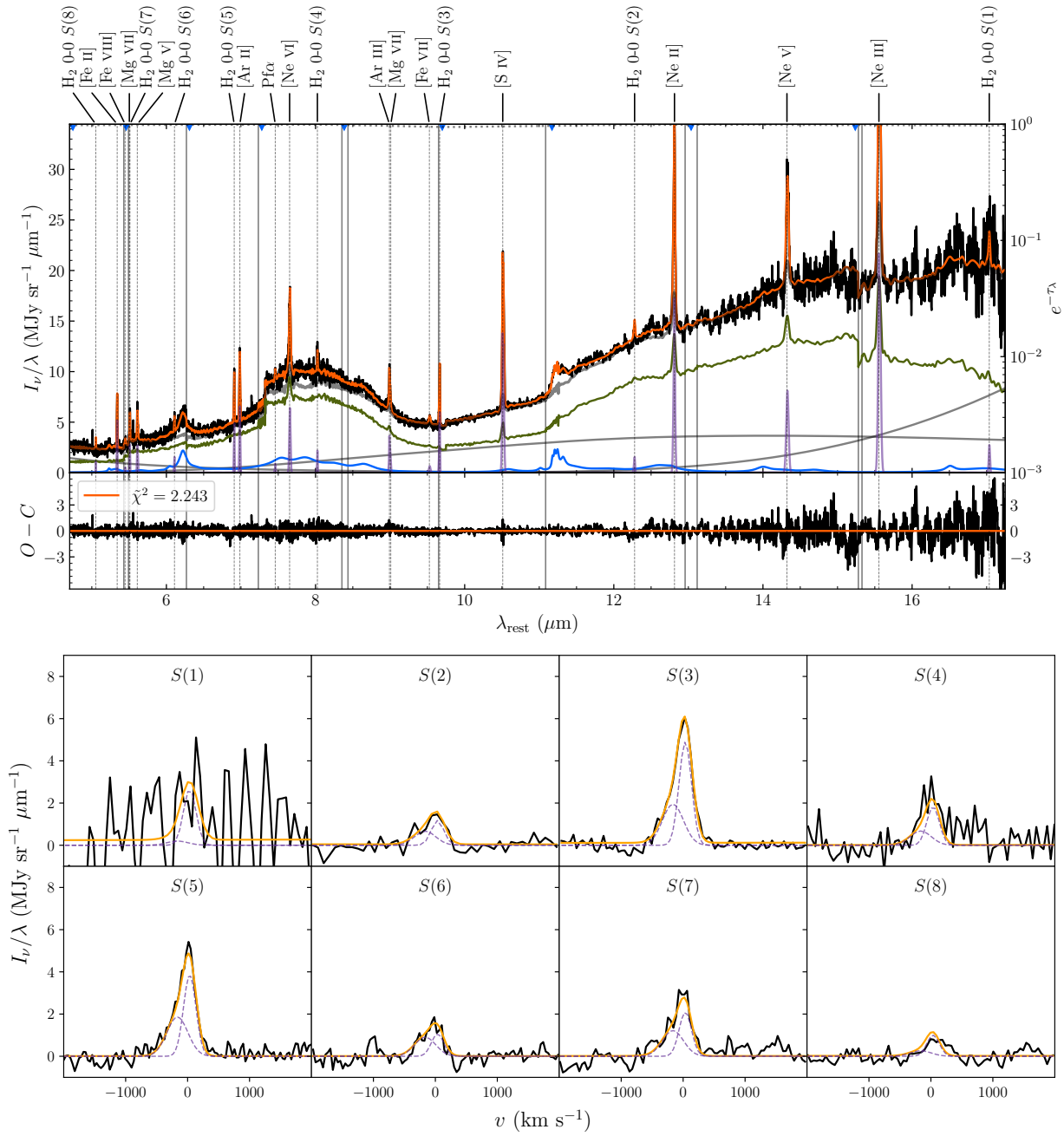

Figure 1. The MIRI/MRS spectrum of a bright off-nuclear spaxel. The spaxel has coordinates (x = 23, y = 16), corresponding to ($\alpha = 23^{\rm h}44^{\rm m}44^{\rm s}.02$, $\delta = -42°43'12''.19$) and a side length of $0''.17$. Top panel: the upper panel shows the data, model, and individual model components, and the lower panel shows the residuals. The data is presented in black, the full model in orange, thermal dust continua in gray, PAH emission in blue, emission lines in purple, and the QSO point-spread function (PSF) model in green. The extinction profile is shown by the gray dotted line across the top of the plots and is read from the right axis. Emission lines are labeled with vertical dashed lines, and boundaries between MIRI/MRS channels are labeled with blue triangles at the top of the plots. This plot shows the full mid-infrared (MIR) spectrum, incorporating data from channels 2–4. The vertical jumps that occur in the QSO PSF component are due to differences in the size and shape of the PSF between MIRI/MRS channels. Bottom panel: a zoom-in of the same spectrum around each of the H_2 emission lines, showing their velocity profiles. As in the top plot, the data is in black, and the model is in orange, with individual velocity components shown with thin purple dashed lines. The continuum model has been subtracted in these zoomed-in plots to highlight the line profiles.

the continuum and higher ionization lines, the H_2 lines have a much smaller equivalent width in the QSO spectrum compared to the host galaxy, so their fluxes are dominated by their host galaxy fluxes away from the nucleus. Most of these lines are unaffected by extinction, but there is one—the H_2 0-0 $S(3)$ line—that fortuitously lands very near the peak of the 9.7 μm silicate absorption feature (see Figure 1). We therefore use the $S(4)/S(3)$ line ratio as a proxy for the extinction. We estimate what this ratio should intrinsically be in the absence of extinction by fitting excitation models with the $S(3)$ line masked out (see Section 3.1.3). We then compare this to our observed $S(4)/S(3)$ ratio to obtain an estimate of the optical depth at the peak of the silicate absorption feature:

$$\tau_{9.7} \approx \ln \frac{[S(4)/S(3)]_{\rm observed}}{[S(4)/S(3)]_{\rm intrinsic}}. \quad (1)$$

Similar techniques have been used in previous studies (i.e., D. Rosenthal et al. 2000), including recently in observations of

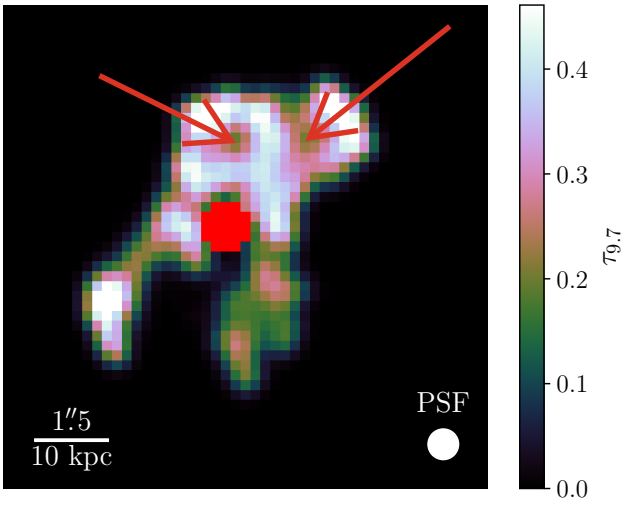

Figure 2. The optical depth of the Phoenix cluster at 9.7 μm from the silicate absorption feature, estimated using the H_2 line ratios. Note that the central spaxels are masked out (denoted by red) since the H_2 lines are not significantly detected in these spaxels. The red arrows highlight two loop structures to the north of the nucleus that have not been seen (or resolved) in dust maps traced by the Balmer decrement or UV continuum.

the Orion Bar and young stellar objects (Ł. Tychoniec et al. 2024; D. Van De Putte et al. 2024). This results in the optical depth map shown in Figure 2. Note once again that this is the optical depth just in the host galaxy, and does not accurately represent the obscuration of the QSO at the center (marked by the red spaxels). The estimated uncertainty in these measurements is $\simeq$5% in the brightest spaxels, rising up to a median of $\simeq$20% in all spaxels, due to a combination of uncertainties in the measured and modeled line ratios.

The optical depth at 9.7 μm is a direct tracer of the column density of silicate dust grains, which create broad absorption features in the MIR through bending and stretching modes. We can see that the silicates are concentrated north of the nuclear region where they form two loop structures (marked with red arrows), with two filaments extending to the south and southeast. The overall structure is reminiscent of the $E(B-V)$ maps obtained from the UV continuum (M. McDonald et al. 2013) and Balmer lines (M. McDonald et al. 2014), showing that the silicate dust grains generally follow the rest of the dust, but the substructure in the silicates is distinct, particularly in the loops. The structure is statistically significant given our relatively low uncertainties in the brighter spaxels.

3.1.2. The Molecular Gas Phase

After obtaining the optical depth map from the excitation models, we run a second iteration of our individual channel fits while locking the optical depth of the host galaxy to these values, with the primary purpose of obtaining more accurate molecular H_2 line fluxes. Note that this analysis inherently assumes that the extinction of the line-emitting H_2 gas is the same as the extinction of the thermal continuum-emitting dust. Previous studies from S. Veilleux et al. (2009) have suggested that there may not be a simple 1:1 correlation between these two optical depths, with the emission lines and PAHs being systematically extincted at lower optical depths than the continuum. We find that due to the low continuum level of the host galaxy relative to the QSO, we require some external constraint on the optical depth parameter to keep it within a parameter space that makes physical sense, and this assumption does not significantly hinder our fitting results. Throughout the rest of our analysis, we are primarily concerned with using optical depths to correct the flux values of emission lines, so the values derived using the $S(4)/S(3)$ line ratios are the most relevant and accurate ones to use.

The flux, velocity width, and velocity shift of the $S(3)$ line are shown in Figure 3. The line is decomposed into two Gaussian velocity components with distinct centers and widths —the leftmost column shows the combined values of both components, the middle column shows the brighter component, and the rightmost column shows the dimmer component. The FWHM of the MIRI/MRS line-spread function, which ranges from $\sim$80–200 km s^{-1} (A. Labiano et al. 2021), has been subtracted in quadrature from all line width measurements. The morphology of the H_2 lines in Figure 3 strongly resembles the CO emission from H. R. Russell et al. (2017), but the H_2 appears slightly more extended than the CO. We compare these morphologies by showing CO contours on top of the H_2 emission in Figure 4. The size of the MIRI/MRS PSF at the wavelength of the $S(3)$ line is roughly the same as the Atacama Large Millimeter/submillimeter Array (ALMA) PSF at the wavelength of CO(3–2) ($\sim$0.″6). However, the H_2 appears more extended due to the difference in sensitivity of the two instruments. The ALMA observations report an uncertainty $\sigma = 0.067$ Jy beam^{-1} km s^{-1}=5.76 $\times$ 10^{-20}erg s^{-1} cm^{-2} spaxel^{-1}. Using the integrated H_2-to-CO ratio over the whole field of view (FOV), this translates to a 3σ lower limit of $10^{-16.83}$erg s^{-1} cm^{-2} spaxel^{-1}, which roughly aligns with the outer CO contour in Figure 4. Therefore, we can conclude that the difference in extent is likely a sensitivity effect and not physical. The H_2 and CO both share three filamentary structures extending to the southeast, south, and northwest, and a bright extended nuclear region. In the core region immediately surrounding the nucleus, the brighter H_2 component has broader line widths of up to 600 km s^{-1} and smaller velocity shifts within $|v| \lesssim 200$ km s^{-1}. It follows that this component primarily traces the motions of unresolved clouds drifting slowly within the turbulent atmosphere of the cluster. Their motions are dominated by large-scale turbulence (e.g., on the scale of a star-forming region) induced by stellar and AGN feedback, with subdominant bulk motions. The dimmer component, which is only significantly detected within this core region, is narrower, with line widths of $\sim$200–300 km s^{-1}, and with faster shifts up to $\pm$400 km s^{-1}. This indicates that this component is capturing the bulk motion of high-velocity gas clouds, which may originate in the filaments that feed into or out of the nucleus, fueling episodes of chaotic cold accretion (see, i.e., M. Gaspari et al. 2018). Moving away from the core region, along these three filaments, the velocity profile becomes dominated by a single component with generally low FWHM ($\sim$100–300 km s^{-1}) and low shifts ($|v| \lesssim 200$ km s^{-1}). This may in fact be the natural extension of the high-velocity component in the core, if our interpretation that this component traces gas feeding in from the filaments is correct. The other H_2 lines generally follow the same morphology as the $S(3)$ line, with varying levels of brightness. We see overall that the warm molecular gas shows a similar morphology to UV and optical continuum emission (M. McDonald et al. 2013, 2015) and warm ionized nebular emission (i.e., [O II], Hβ in M. McDonald et al. 2014), tracing regions of rapid and recent star formation. Figure 4 also

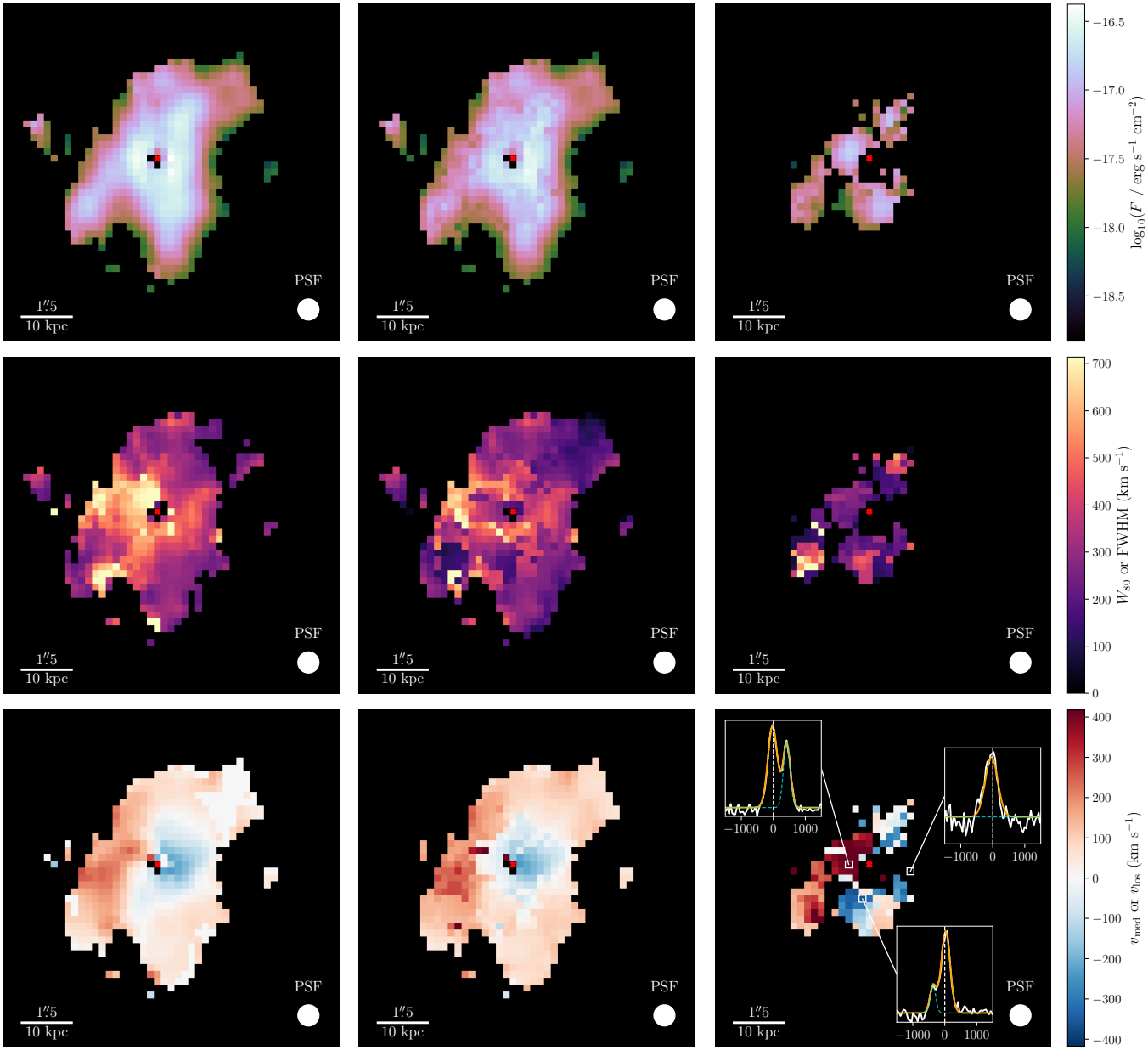

Figure 3. Maps of the H_2 0–0 $S(3)$ line over the channel 3 field of view (FOV). The top row shows the flux with a logarithmic color map. The left panel is the total flux, and the right two panels show the flux of the individual components. The middle row shows the line width in kilometers per second. The left panel is W_{80}, the width containing 80% of the flux, and the right two panels are the FWHMs of the individual components. The bottom row shows the line-of-sight (LOS) velocity in kilometers per second. The left panel is the median velocity, and the right two panels are the LOS velocities of the individual components. In all of the middle- and right-column panels, the components are sorted by flux, with the middle column having the larger flux and the right column having the smaller flux. Only spaxels with a signal-to-noise ratio (S/N) $\geqslant 3$ are shown. In the bottom-right panel, the inset panels show the velocity profiles of the line at the indicated spaxel locations. In each inset, the white vertical dashed line shows the velocity zero-point, and the cyan dashed line shows the individual velocity component, which corresponds to the value shown in this map.

shows that the molecular gas wraps around the cavities in the X-ray emitting ICM (magenta dashed contours), inflated by the quasar's radio jets (red contours). The H_2 gas is possibly being uplifted in the bubble's turbulent wakes or forming in situ through turbulent mixing at the boundaries of the bubbles (M. McDonald et al. 2015, R25).

3.1.3. Molecular Gas Mass

Using the fluxes for the set of pure rotational H_2 lines that fall within our wavelength range, $S(1)$ to $S(8)$, we construct excitation diagrams of the upper level column densities of these transitions and fit a continuous temperature model from A. Togi & J. D. T. Smith (2016):

$$\frac{N_u}{g_u} = \frac{N_{\rm tot}(n-1)}{T_\ell^{1-n} - T_u^{1-n}} \int_{T_\ell}^{T_u} \frac{e^{-E_u/kT}}{Z(T)} T^{-n} dT \quad (2)$$

where N_u, E_u, and g_u are the column density, energy, and degeneracy of the upper energy level, T_ℓ and T_u are the limits of the temperature distribution, $N_{\rm tot}$ is the total column density of H_2, $Z(T)$ is the partition function of the H_2, and n is a generic power-law index that sets the temperature distribution. We set $T_u = 2000$ K following A. Togi & J. D. T. Smith (2016) and allow $N_{\rm tot}$, n, and T_ℓ to vary.

We have two goals with this analysis: (1) obtain "intrinsic" $S(4)/S(3)$ line ratios so that we may reconstruct the optical

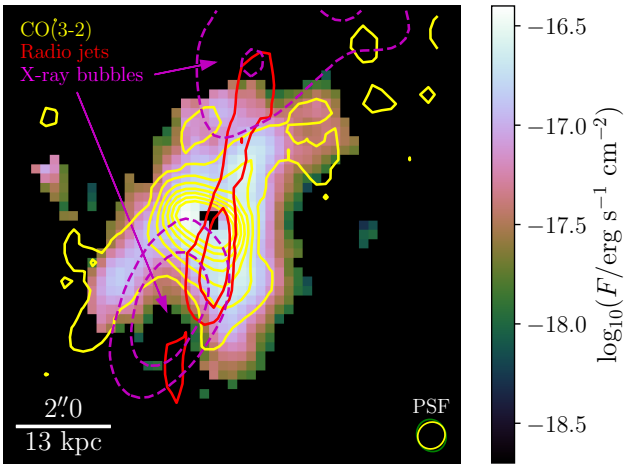

Figure 4. A map of the H_2 0–0 $S(3)$ flux (identical to the top-left panel of Figure 3). CO emission from Atacama Large Millimeter/submillimeter Array (ALMA) observations (H. R. Russell et al. 2017) is shown with the yellow contours (ranging from 0σ–7σ above the mean). Radio jets from Very Large Array observations (R. Timmerman et al. 2021) are shown with the red contours (at 2σ and 4σ above the background). X-ray cavities from Chandra observations (M. McDonald et al. 2019) are shown in the magenta dashed contours (at 2σ and 4σ below the mean). The PSF shapes of MIRI/MRS and ALMA are both shown in the bottom-right corner, with MIRI in green and ALMA in yellow. Both have FWHMs of ∼0.″6.

depth of the emission lines in the host galaxy; and (2) obtain an estimate for the total molecular gas mass and how this gas is distributed spatially. For the first goal, we take the H_2 line fluxes from our first iteration fits and mask the $S(3)$ line. Once we obtain a modeled value for the $S(3)$ line, we can compute the inferred line ratio as

$$\frac{F_i}{F_j} = \frac{N_i}{N_j}\frac{\lambda_j}{\lambda_i}\frac{A_i}{A_j} \tag{3}$$

where F_i, N_i, λ_i, and A_i are the fluxes, column densities, wavelengths, and Einstein A coefficients of each line. We then compare this with the observed line ratio to compute an optical depth as described in Section 3.1.1. After obtaining the optical depth map, we use line fluxes from our second iteration fits, including the $S(3)$ line, to obtain estimates for the molecular gas mass. Note that we use the total flux of the H_2 lines in both of these procedures, recombining the components from the QSO PSF and host galaxy decomposition. The decomposition into these two components is still important, however, since they may be extincted by different amounts (this is only relevant for the $S(3)$ line, so it is not an important distinction for the first goal). Note that including the rotational lines up to $S(8)$ limits us to the channel 2 FOV.

We show the excitation diagram for the H_2 rotational lines, integrated over the whole FOV of channel 2, in the left panel of Figure 5. The errors here have been obtained by bootstrapping the spectral fits 100 times, so they are purely statistical. The data are well fit by a temperature distribution with a power-law index of $n = 4.7 \pm 0.1$ and a lower temperature limit of $T_\ell = 44^{+143}_{-5}$ K. The large upper uncertainty on T_ℓ indicates that the model loses sensitivity to H_2 at temperatures $\lesssim$200 K (see A. Togi & J. D. T. Smith 2016). However, the continuous temperature model allows us to extrapolate to lower temperatures and get an estimate of the total molecular gas mass. We use a lower temperature limit appropriate for ultraluminous infrared galaxies (ULIRGs) and LIRGs of $T'_\ell = 80$ K (A. Togi & J. D. T. Smith 2016), which yields a total molecular gas mass of $M_{H_2} = 1.9^{+0.5}_{-0.4} \times 10^{10}\,M_\odot$. This is in excellent agreement with previous measurements from M. McDonald et al. (2014) and H. R. Russell et al. (2017), who obtained an H_2 mass of $2.1 \pm 0.3 \times 10^{10}\,M_\odot$ using a CO-to-H_2 conversion factor $X_{CO} = 0.4 \times 10^{20}\,\mathrm{cm^{-2}\,(K\,km\,s^{-1})^{-1}}$, equivalent to α_{CO}= $0.86\ M_\odot\ \mathrm{pc^{-2}\,(K\,km\,s^{-1})^{-1}}$. Spaxel-by-spaxel fits of these models, with the molecular gas mass in each spaxel, are shown in the right panel of Figure 5. The mass distribution generally follows the same morphology as the surface brightness.

By comparing the H_2 mass measurements of H. R. Russell et al. (2017) to ours, assuming the same underlying CO mass, we can obtain an estimate of the CO-to-H_2 conversion factor of $\alpha_{CO} = 0.8 \pm 0.2\ M_\odot\ \mathrm{pc^{-2}\,(K\,km\,s^{-1})^{-1}}$. This is roughly a factor of 5 smaller than the standard Milky Way disk value of $\alpha_{CO,Gal} = 4.3\ M_\odot\ \mathrm{pc^{-2}\,(K\,km\,s^{-1})^{-1}}$ (A. D. Bolatto et al. 2013). Lower values of α_{CO} are common in mergers, ULIRGs, and starburst galaxies because these systems tend to have more turbulence and gas inflows, which lead to molecular gas at higher temperatures and densities. This increases the molecular gas luminosity per unit mass, lowering α_{CO} (D. Downes et al. 1993; D. Downes & P. M. Solomon 1998; A. Togi & J. D. T. Smith 2016). The extreme cooling and star formation in Phoenix make it comparable to these systems and are the most likely explanation behind the lowered α_{CO} value. Variations in metallicity can also produce differences in the conversion between CO and H_2, and are likely the reason that our H_2 mass measurement does not match exactly with H. R. Russell et al. (2017; aside from pure statistical variations).

We also compare these measurements of the total (cold) molecular gas mass to the (warm) molecular gas mass traced by the MIR H_2 transitions by fitting a discrete two-temperature model with no extrapolation. This results in a warm H_2 mass of $3.4 \pm 1.4 \times 10^8\,M_\odot$ at characteristic temperatures of 350^{+40}_{-30} K and 1100 ± 100 K. The fit quality is marginally worse than the continuous temperature model, with a $\tilde{\chi}^2 = 1.63$. This implies that the warm H_2 accounts for only a very small fraction (∼2%) of the total H_2 mass, which is to be expected based on the mass distributions for the A. Togi & J. D. T. Smith (2016) models ($dM/dT \propto T^{-n}$). Indeed, the warm H_2 mass fraction estimated from these models, using a lower temperature limit $T_\ell = 200$ K (from the sensitivity floor of the continuous model) relative to a lower integration temperature $T'_\ell = 80$ K, is of a similarly small magnitude:

$$\frac{\int_{T_\ell}^{T_u}(dM/dT)dT}{\int_{T'_\ell}^{T_u}(dM/dT)dT} \approx \left(\frac{T_\ell}{T'_\ell}\right)^{1-n} \approx 3\%. \tag{4}$$

3.1.4. PAH Features

Due to a rather unfortunate alignment in the wavelength boundaries between channels of the MIRI instrument, at the redshift of the Phoenix cluster, the prominent PAH features at 7.7 μm and 11.3 μm both land at the edges between channels 2/3 and 3/4, meaning they are partially cut off in each channel. This motivated us to, in addition to our single-channel fits, also run a multichannel fit by combining data from channels 2–4, projecting everything onto the channel 2 grid. This way, we are able to measure the full integrated fluxes of these PAH features.

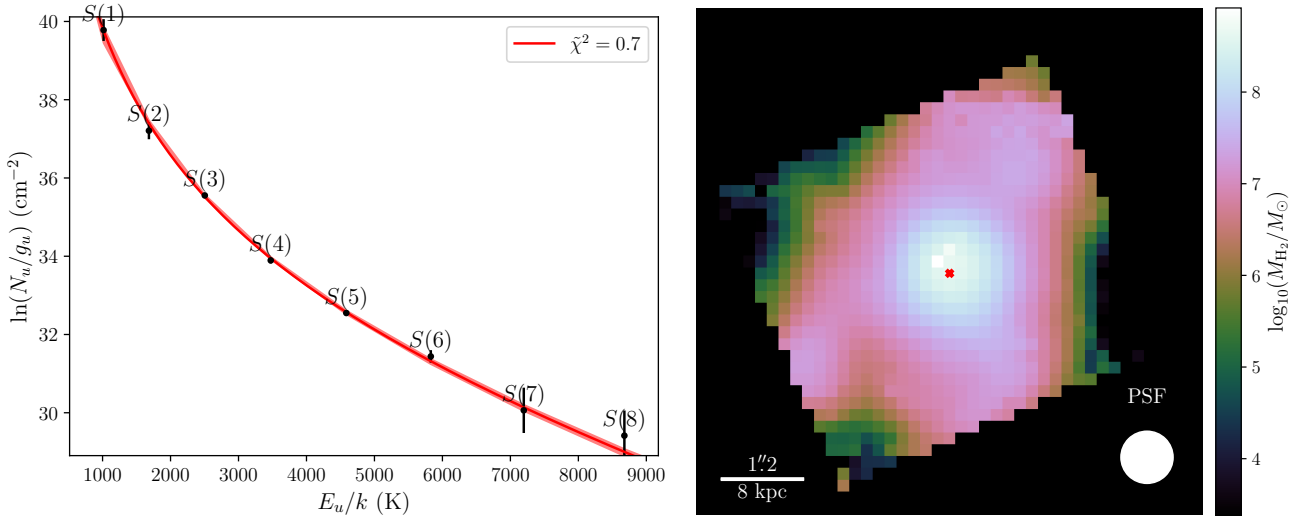

Figure 5. Left panel: an excitation diagram of the H_2 rotational lines integrated over the full channel 2 FOV. The abscissa is the energy of the upper level of the transition in kelvin, E_u/k, and the ordinate is the column density of the upper level of the transition in cm^{-2}, N_u, normalized by the degeneracy g_u. The black points show the observed values, with each H_2 line labeled accordingly, and the red line shows the best-fit continuous temperature model, with a $\tilde{\chi}^2 = 0.7$. Right panel: a map of the total molecular gas mass over the channel 2 FOV, obtained by fitting a continuous temperature model to the H_2 excitation diagram, extrapolating to lower temperatures, and integrating over temperature. Note that the color scale is logarithmic (base 10).

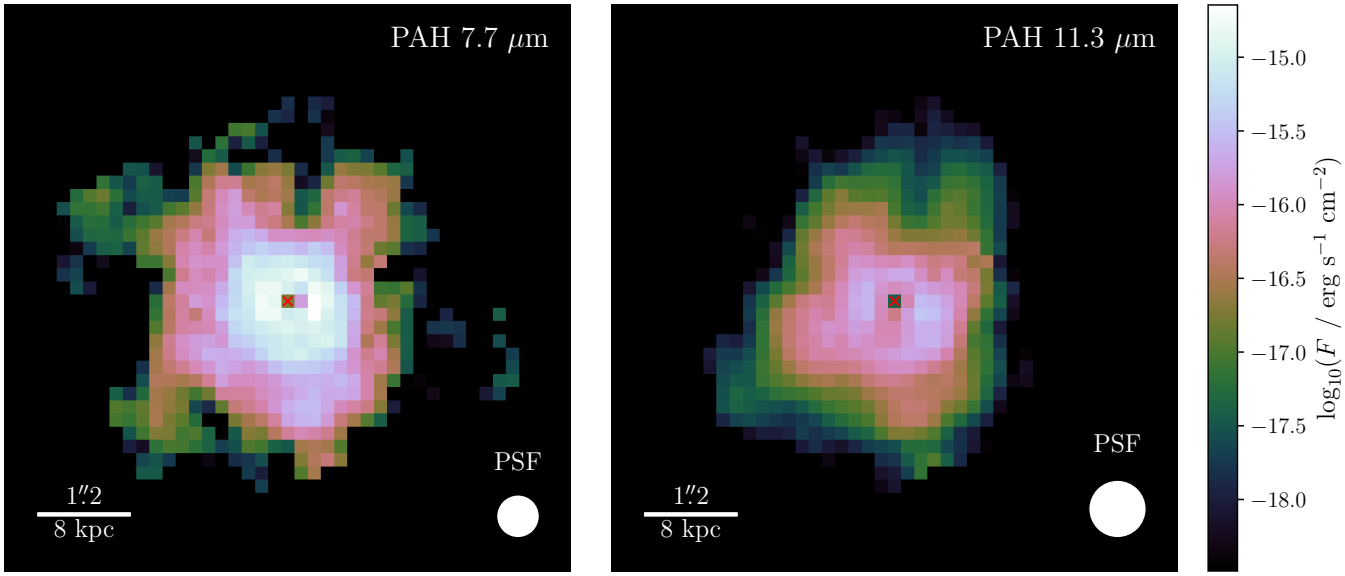

Figure 6. Maps of the 7.7 μm and 11.3 μm PAH features over the channel 2 FOV.

Maps of the total flux of the 7.7 μm and 11.3 μm PAH complexes are shown in Figure 6. The PAH emission is more centrally concentrated than the molecular gas and does not have distinct filaments extending to the south and southeast, but it does have protrusions from the nucleus that generally align with the directions of the filaments. However, we are cautionary in drawing any conclusions from the morphology of these protrusions, as they may be partially contaminated by PSF residuals that have not been fully subtracted. This is likely due to the low equivalent widths of the PAH features in this system, making it difficult for our spectral modeling procedure to cleanly separate the PAH features from the continuum and PSF. Despite these shortcomings, we can argue that the PAH morphology is clearly extended to both the north and the south, whereas the warm/hot ionized gas phases at $\sim 10^{5.5}$ K are only extended to the north (see, i.e., R25). Qualitatively speaking, then, the PAHs more closely resemble the morphologies of the colder gas phases. The physical extent of the PAHs is likely constrained by the necessity for them to be shielded from hard ionizing UV and X-ray photons from the AGN, and photons and suprathermal electrons from the hot ICM. It is interesting, then, that we still see significant PAH emission even in the central-most spaxels closest to the X-ray-luminous AGN. This seems to be a ubiquitous feature of AGNs—they may have profound effects on the PAH grain size distribution and ionization fraction, preferentially destroying smaller and more ionized grains, but they seemingly do not cause the unilateral destruction of PAHs (see, i.e., I. García-Bernete et al. 2024). The highly obscured nature of Phoenix's AGN may also play a role in the survivability of PAHs within such close distances. We explore this further in Section 4.1.4.

Table 1
CIGALE Parameters

Parameter Description	Name	Searched Values	Bayesian Fit Value
Star formation history	sfhdelayed	⋯	⋯
Main population e-folding time	tau_main	100, 500, 1000, 2000, 4000, 6000, 8000 Myr	6000 ± 2000 Myr
Main population age	age_main	8000 Myr	⋯
Burst population e-folding time	tau_burst	1, 10, 100, 1000 Myr	600 ± 400 Myr
Burst population age	age_burst	1, 5, 10, 20, 50, 100 Myr	26 ± 13 Myr
Burst population mass fraction	f_burst	0, 0.0001, 0.0005, 0.001, 0.005, 0.01	0.006 ± 0.002
Stellar populations	bc03	⋯	⋯
Initial mass function	imf	Salpeter	⋯
Stellar metallicity	metallicity	0.0004, 0.004, 0.008	0.006 ± 0.002
Old and young population separation age	separation_age	10 Myr	⋯
Nebular emission	nebular	⋯	⋯
Ionization parameter	logU	−3	⋯
Gas metallicity	zgas	0.005	⋯
Electron density	ne	1000 cm^{-3}	⋯
Lyman continuum dust absorption fraction	f_dust	0, 0.001, 0.01, 0.1	0.01 ± 0.02
Line width	lines_width	800 km s^{-1}	⋯
Dust attenuation	dustatt_modified_starburst	⋯	⋯
Gas reddening	E_BV_lines	0.1, 0.2, 0.3, 0.4, 0.5, 0.6, 0.7	0.500 ± 0.002
Stellar reddening reduction factor	E_BV_factor	0.44	⋯
UV bump amplitude	uv_bump_amplitude	0	⋯
Attenuation curve power-law slope modifier	powerlaw_slope	0	⋯
Dust emission	dl2014	⋯	⋯
PAH mass fraction	q_pah	0.47	⋯
Minimum radiation field	umin	10	⋯
Power-law slope	alpha	2	⋯
Illumination fraction	gamma	0.25	⋯
AGN	skirtor2016	⋯	⋯
Average edge-on optical depth at 9.7 μm	t	9	⋯
Dust density radial slope	pl	1	⋯
Dust density polar slope	q	0	⋯
Torus opening angle	oa	50°	⋯
Ratio of outer to inner radius	R	30	⋯
Inclination angle	i	60°, 70°, 80°, 90°	80° ± 1°
Optical disk power-law slope modifier	delta	1.0	⋯
AGN fraction of IR luminosity	fracAGN	0, 0.1, 0.2, 0.3, 0.4, 0.5, 0.6, 0.7, 0.8, 0.9, 0.99	0.50 ± 0.01
Polar dust extinction	EBV	0, 0.2, 0.4	0.21 ± 0.05
Radio emission	radio	⋯	⋯
FIR/radio correlation coefficient	qir_sf	2.7	⋯
Star formation synchrotron slope	alpha_sf	0	⋯
AGN radio-loudness	R_agn	0.1, 1, 10, 100, 1000	10
AGN radio emission slope	alpha_agn	1.35	⋯

Note. Any parameters not listed here take their default values.

3.2. Stellar Populations and a Robust SFR

With these new JWST data in the MIR, we obtain valuable constraints on the shape of Phoenix's spectral energy distribution (SED) in a region that is dominated by the AGN and thermal dust emission. As such, we calculate the integrated flux within each subchannel (using a consistently sized aperture, which takes up the full FOV of channel 1) and create simulated broadband photometry measurements. We combine these measurements with archival broadband data spanning from the UV to the radio (GALEX, Hubble Space Telescope, Two Micron All Sky Survey, WISE, Herschel/PACS, and Herschel/SPIRE; M. McDonald et al. 2012; ATCA and SUMSS; M. McDonald et al. 2014) and fit SED models using the CIGALE software (M. Boquien et al. 2019; G. Yang et al. 2020).[23] The modules used and parameter space searched are detailed in Table 1. The full range of parameters

[23] CIGALE website

we wished to search was large enough that doing a single run varying everything at the same time would have been computationally infeasible. As such, we took an iterative approach and varied parameters in groups. The values shown in Table 1 for the nebular, dust, AGN, and radio modules that are fixed have been selected from previous iterations. During these iterations, the other parameters are given values based on educated guesses of the conditions in Phoenix A—for example, given that it hosts a bright type II AGN, we assumed an inclination angle of 70° and an AGN fraction of 50%. In most cases, we see that the final values of these parameters in our final fits are not too far from these initial guesses. The new JWST points in the MIR provide stronger constraints on the shape of the AGN and dust emission, allowing us to adjust many of the AGN torus parameters from their default values. However, a major strength of CIGALE comes from its ability to constrain parameters in different wavelength bands using the principles of energy balancing and correlations between parameters from the underlying physics. This is why, in our final iteration, we still allowed certain parameters in these modules to vary from their previously found values, such as the AGN fraction and radio-loudness.

A notable caveat to this analysis is the spatially agnostic nature of the CIGALE fit, which presents itself most prominently in the decomposition between the "dust emission" and "AGN" components of the model. The templates CIGALE uses for dust emission only consider starlight-heated dust, whereas a powerful AGN such as the one in Phoenix may also contribute to heating the dust all throughout the host galaxy. In contrast, the SKIRTOR AGN templates only consider the radiative transfer process through the dust in the nucleus/torus region, not throughout the whole galaxy. A study from S. Viaene et al. (2020) looking at NGC 1068 showed, using their own radiative transfer analysis, that considering the effects of the AGN separately caused it to contribute up to 15% of the total dust heating, depending on viewing angle. In the case of Phoenix, with a much more luminous AGN, this fraction could be even higher. Nevertheless, we expect the ramifications of this on our interpretation of the results to be minor: S. Viaene et al. (2020) performed comparison CIGALE fits and found the SFRs to be in agreement with their models. Without the inclusion of an AGN component, they found the young stellar populations to be overly attenuated in order to boost the MIR dust emission to the observed levels, but in our case, the separate inclusion of an AGN component with a distinct shape in the MIR likely alleviates this concern.

The final SED model is shown in Figure 7. The attenuated stellar populations (blue) dominate in the UV and optical due to the obscuration of the AGN, while the AGN (purple) and dust emission (brown) dominate in the MIR to far-IR (FIR). The data from ∼5 to 10 μm in the observed frame (MIRI channels 1 and 2) provide the strongest constraints on the relative power of the AGN and dust emission, since dust emission in this range would correspond to dust heated above $\gtrsim$300 K, which is difficult to achieve without the presence of an AGN. Notice that the AGN component dominates the SED in this range, whereas the dust emission becomes the dominant component in the FIR above ∼100 μm, corresponding to much colder (∼30 K) temperatures. Interpolating our model at a rest-frame wavelength of 24 μm gives a total luminosity of $\nu L_\nu(24\,\mu\mathrm{m}) \approx 3.0 \times 10^{46}\,\mathrm{erg\,s^{-1}}$ and an AGN-subtracted (i.e., host galaxy) luminosity of $\approx 1.3 \times 10^{46}\,\mathrm{erg\,s^{-1}}$. We will use these values in the next section for a more in-depth analysis of the heating mechanisms of the different gas and dust phases.

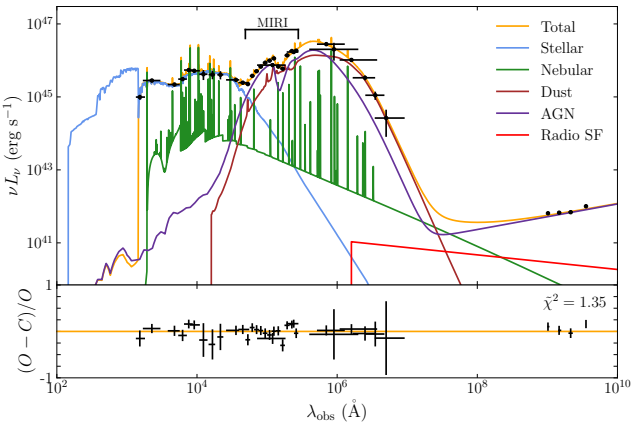

Figure 7. The best-fit SED model for Phoenix A. Photometry data points are shown in black with error bars. The full SED model spectrum is the amber line, and the individual components of the SED are labeled in the legend. The bottom panel shows the residuals of the fit.

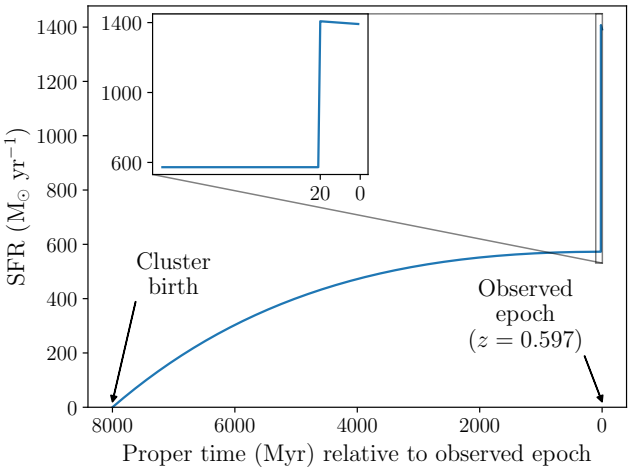

Figure 8. The star formation rate (SFR) is shown as a function of time in Phoenix's rest frame, relative to the observed epoch. As the main "old" stellar population has an age fixed at 8 Gyr, the farthest back the plot goes is 8 Gyr relative to the observed epoch (corresponding roughly to the Big Bang). An inset is shown zooming in on the most recent 100 Myr of star formation, showing the rapid spike at 20 Myr. The shape of the star formation history is flexible aside from the late-time burst.

The star formation history is shown in Figure 8. The models settle on a fairly consistent SFR throughout the past 8 Gyr of the galaxy's history, with the average SFR over all time being around 400 $M_\odot$ yr^{-1}. The recent burst of star formation started 26 ± 13 Myr ago and marginally favors models with large e-folding times of 600 ± 400 Myr, bringing the current instantaneous value of the SFR well above 1000 $M_\odot$ yr^{-1}. The exact shape of the star formation history is not well constrained by the photometry, which is evident in the large uncertainties of the e-folding times for both the main and burst populations. The data could be nearly equally well described by, for example, a model with a more heavy weighting toward stars that formed earlier (corresponding to shorter e-folding times). This may have an effect on the relative old and young population masses that we measure, but it will have a minimal effect on the long-time averaged SFRs. These values are summarized in Table 2, along with other parameters of the star

Table 2
CIGALE Stellar Population Parameters

Parameter	Symbol	Value
Old population age	$t_{*,\mathrm{old}}$	8 Gyr
Young population age	$t_{*,\mathrm{young}}$	26 ± 13 Myr
Old population mass[a]	$M_{*,\mathrm{old}}$	$2.6 \pm 0.5 \times 10^{12}\,M_\odot$
Young population mass[a]	$M_{*,\mathrm{young}}$	$1.3 \pm 0.1 \times 10^{10}\,M_\odot$
Stellar metallicity	Z_*	0.006 ± 0.002
Instantaneous SFR[b]	SFR	$1330 \pm 130\,M_\odot\ \mathrm{yr}^{-1}$
10 Myr averaged SFR[b]	$\langle \mathrm{SFR} \rangle_{10}$	$1340 \pm 100\,M_\odot\ \mathrm{yr}^{-1}$
100 Myr averaged SFR[b]	$\langle \mathrm{SFR} \rangle_{100}$	$740 \pm 80\,M_\odot\ \mathrm{yr}^{-1}$

Notes. All measured stellar masses and SFRs assume a Salpeter IMF.
[a] To convert stellar masses to those that would be measured with other IMFs, multiply by 0.61 (Chabrier) or 0.66 (Kroupa; P. Madau & M. Dickinson 2014).
[b] To convert SFRs to those that would be measured with other IMFs, multiply by 0.63 (Chabrier) or 0.67 (Kroupa; P. Madau & M. Dickinson 2014).

formation history, which are derived from the parameters given in Table 1. The fact that the late-time burst occurs within $\lesssim$20 Myr suggests that even the youngest O-type stars with lifetimes $\leqslant$10 Myr should be present in the galaxy. The presence of extremely luminous O-type stars explains why, despite the young population contributing a considerable amount to the observed optical/UV luminosity, it only contributes $\sim$0.5% of the total stellar mass.

4. Discussion

4.1. Gas and Dust Energetics

D11 studied a sample of cool core (CC) BCGs and found that the thermal dust continuum and PAH features were consistent with being heated primarily by star formation, whereas the warm molecular H_2 gas and ionized [Ne II] gas required an additional heating source, which they attributed to energetic particles from the ICM. It is useful to reexamine some of these correlations with the Phoenix cluster in mind, for a few reasons: (1) To understand the relative contributions of different heating sources in Phoenix itself, and compare them to the typical cool core population; (2) To isolate the effects of AGN photoionization heating, since none of the BCGs studied in the D11 sample exhibited evidence of AGN activity; and (3) To identify the relative importances of different heating sources in offsetting cooling flows.

4.1.1. Rotational H_2 Emission

Being the gas phase most closely linked to star formation, cold molecular gas is an important tool in studying the characteristics of star-forming regions. However, it is often difficult to detect directly, as cold molecular H_2 does not emit strongly, and must be traced by the second-most abundant molecule in the interstellar medium (ISM), CO, instead. Warm molecular gas heated to a few 100 K—a few 1000 K, on the other hand, has rovibrational emission lines in the infrared that can be used to directly detect the warm H_2 gas, but no longer has the direct connection to star formation due to its increased excitation. Untangling how much of this emission is due to star formation, as opposed to other sources, can be an important clue in distinguishing Phoenix from other BCGs. In the D11 sample of BCGs, the ratio of the combined luminosity of the H_2 0–0 $S(2)$ and $S(3)$ lines (L_{H_2}) and the 24 μm continuum

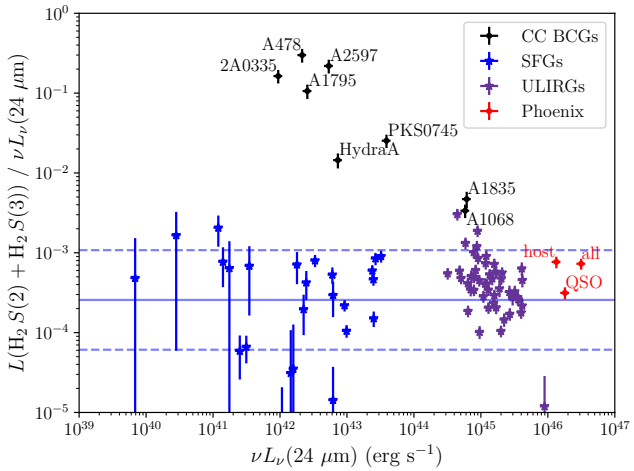

Figure 9. The ratio of the combined H_2 0–0 $S(2)$ and $S(3)$ luminosity over the 24 μm continuum luminosity $\nu L_\nu(24\ \mu\mathrm{m})$ plotted as a function of $\nu L_\nu(24\ \mu\mathrm{m})$. The black points show the cool core (CC) BCGs from the D11 sample, and the red points show the Phoenix cluster: "all" corresponds to the integrated values over the whole FOV, "host" corresponds to the integrated values after the QSO PSF has been subtracted, and "QSO" corresponds to the integrated QSO PSF values. The blue stars show galaxies from the SINGS sample designated as "H II" or star-forming galaxies (SFGs) by J. D. T. Smith et al. (2007). The solid blue line shows the average value of these galaxies, and the dashed blue lines show the 1σ standard deviation. The purple stars show ULIRGs from D. Farrah et al. (2007).

luminosity ($L_{24} \equiv \nu L_\nu$ at 24 μm) was elevated orders of magnitude above typical values seen in star-forming galaxies (M. Treyer et al. 2010; from $\sim 4 \times 10^{-4}$ to as high as 0.3), suggesting that star formation is not a significant heating mechanism, and other energy sources, such as cosmic rays, likely play an important role in the observed H_2 luminosities. However, the massive starburst in the Phoenix cluster gives it the unique position of having emission components comparable to both the BCGs and the star-forming galaxies.

In order to make this comparison, we need a measurement of L_{24} for Phoenix. For this, we take the values interpolated from our CIGALE fit in Section 3.2. Indeed, on average we see a much smaller L_{H_2}/L_{24} ratio of $\sim 8 \times 10^{-4}$. It lies along the anticorrelation between L_{H_2}/L_{24} and L_{24} noted by D11, which is primarily due to its increased L_{24} relative to the other BCGs. We recreate Figure 10(b) from D11 in Figure 9, which shows this anticorrelation. We compare the BCG sample to a sample of nearby infrared-luminous galaxies: the Spitzer Infrared Nearby Galaxies Survey (SINGS), with photometry measurements taken from D. A. Dale et al. (2007), H_2 measurements taken from H. Roussel et al. (2007), and PAH and neon line measurements taken from J. D. T. Smith et al. (2007). We select only the star-forming galaxies (SFGs), designated by the type "H II" by J. D. T. Smith et al. (2007), and show this sample with blue stars in Figure 9. These galaxies have L_{H_2}/L_{24} ratios much smaller than the BCGs and more similar to Phoenix, but with smaller overall L_{24}. We also include a selection of ULIRGs from D. Farrah et al. (2007), with 24 μm fluxes cross-matched from the NASA/IPAC Extragalactic Database (NED; 2019). Powered by vigorous starbursts or AGNs, the ULIRGs bridge the gap between the normal star-forming galaxies and Phoenix. This shows that Phoenix is an extension of this population into the cluster environment—a unique case where a galaxy in the highest-mass regime hosts both a QSO and a starburst. This would seem to imply that the majority of the H_2 emission in Phoenix is produced by stellar

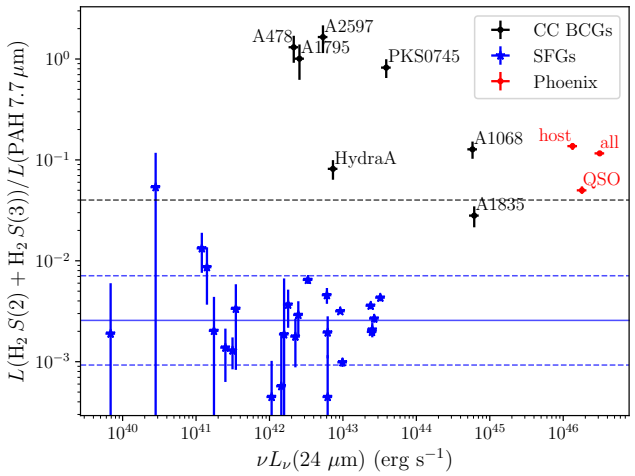

Figure 10. The ratio of the combined H_2 0–0 $S(2)$ and $S(3)$ luminosity over the 7.7 μm PAH feature luminosity, plotted against $\nu L_\nu(24\ \mu\mathrm{m})$. The color-coding of the points is identical to Figure 9. The black dashed line shows the upper limit of the L_{H_2}/L_{PAH} ratio in photodissociation region (PDR) simulations using the Meudon code (F. Le Petit et al. 2006), showing that points above this line must have some nonradiative contribution to their H_2 emission.

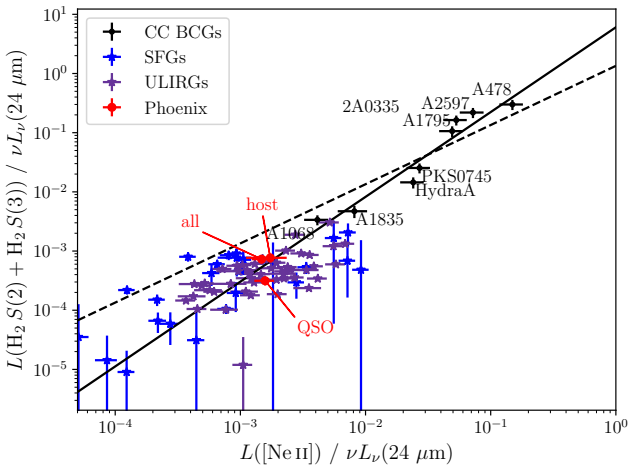

Figure 11. The ratio of the combined H_2 0–0 $S(2)$ and $S(3)$ luminosity over the 24 μm continuum luminosity $\nu L_\nu(24\ \mu\mathrm{m})$ vs. the ratio of the [Ne II] λ12.813 μm luminosity over $\nu L_\nu(24\ \mu\mathrm{m})$. Both luminosities are normalized to $\nu L_\nu(24\ \mu\mathrm{m})$ to remove any "bigger is bigger" effects (R. C. J. Kennicutt 1990). The data points are labeled identically to Figure 9. The dashed line shows a 1:1 correlation, and the solid line shows the best-fit power law, which is marginally steeper.

heating, which would make it unique among the cool core BCGs. However, we must note that the presence of the AGN increases L_{24} substantially above that produced by dust-reprocessed stellar light in the host galaxy. We have attempted to account for this by subtracting the portion of L_{24} generated by the AGN and recovering the L_{24} just from the host galaxy. But as discussed in Section 3.2, if the AGN is a significant source of heating for the dust in the host galaxy and not just the nucleus, this may not be properly separated by our decomposition. If the true value of L_{24} from just starlight is a few times smaller than our analysis shows, this could indicate a nonnegligible elevation of the L_{H_2}/L_{24} ratio, which in turn implies a nonradiative contribution to the H_2 emission (e.g., P. Ogle et al. 2010).

To investigate this, we plot the ratio of H_2 to PAH luminosity, which should be more resistant to the effects of AGN contamination, in Figure 10. This figure reveals that, indeed, the ratio of H_2 to PAH emission in Phoenix is noticeably similar to that of its nearest cool core cluster neighbors, A1068 and A1835. Like these other cool cores, Phoenix appears to have either enhanced H_2 emission or suppressed PAH emission (or both) relative to the pure star-forming galaxies of the SINGS sample, though the effect is not quite as prominent as in the most quiescent cool cores. It is likely that the H_2 emission in Phoenix is boosted by shocks induced by both the mechanical influence of the radio jets from the AGN and from stellar feedback in the form of supernovae. The PAH emission may be suppressed due to grain destruction and sputtering caused by the harsh ionizing radiation from the AGN and the ICM. We investigate both of these possibilities in the next few subsections.

We also see a strong correlation between the H_2 luminosity and the [Ne II] λ12.813 μm luminosity ($L_{[\mathrm{Ne\,II}]}$), corroborating that found in D11 (their Figure 11; our Figure 11). Phoenix lies right along the best-fit power law, $(L_{H_2}/L_{24}) \propto (L_{[\mathrm{Ne\,II}]}/L_{24})^{1.4\pm0.1}$, but lands in a region of parameter space similar to the SINGS star-forming galaxies and ULIRGs as opposed to the other BCGs. This correlation means that the heating sources for the molecular gas and the warm ionized gas must be tightly interlinked. In other words, if the observed H_2 excitation is due to a combination of stellar and shock heating, then the [Ne II] excitation can likely also be attributed to these sources.

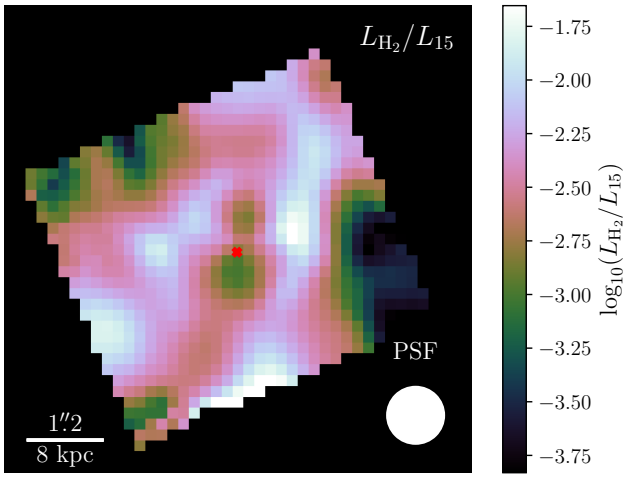

Figure 12. A map of the ratio of the $H_2S(2) + S(3)$ luminosity over the 15 μm continuum luminosity in each spaxel, over the channel 2 FOV. This map has been spatially convolved with a Gaussian with a standard deviation of 1 pixel. Areas with a higher L_{H_2}/L_{15} ratio may have more contributions from shocks and other nonradiative emission mechanisms compared to regions with lower L_{H_2}/L_{15} ratios.

4.1.2. Shock-driven H_2 Emission

Shocks may constitute a significant fraction of the H_2 emission observed in this cluster. To better quantify this contribution, here we examine the H_2 emission in further detail both spatially and spectrally. We show the spatial distribution of the H_2-to-continuum ratio in Figure 12. Note that in this figure we use the 15 μm continuum luminosity, rather than the 24 μm continuum luminosity, since our MIRI/MRS spectral coverage for this system does not extend to 24 μm. Note that 15 μm was chosen as a proxy due to it being relatively free from contamination from lines and PAH features, while not being too short in wavelength that the continuum becomes

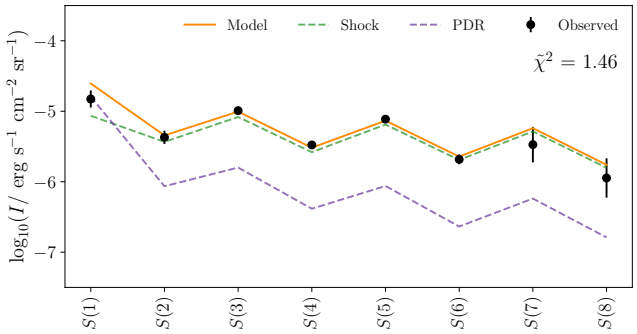

Figure 13. The H_2 line intensities integrated over the whole field of view are shown alongside a toy model that decomposes the emission into two components: shocks (green) and PDRs (purple). The total model is shown in orange. The individual rotational H_2 lines are labeled along the x-axis. Shocks appear to be the predominant emission mechanism for most of the H_2 lines, though the PDR contribution is still important for producing a model that represents the data well, particularly in the $S(1)$ line.

dominated by emission from the AGN and stellar populations. Focusing on the spatial distribution, rather than the absolute value of this ratio, we find that the H_2 emission is enhanced relative to the continuum to the east and west of the nucleus, forming a cocoon-like shape. This may be the result of bowed shock fronts expanding out from the north–south aligned radio jets (see, for example, Figure 3 in G. V. Bicknell et al. 2000).

To constrain how much of the H_2 emission can be attributed to shocks, we implement a two-component toy model that describes the H_2 emission as a combination of shocks (with some distribution over velocities) and photodissociation regions (PDRs). We follow the methods of J. A. Villa-Vélez et al. (2024) in constructing this model. For the PDR component, we use pre-computed models from the Meudon PDR code[24] with a density $n_{\rm H} = 10\,{\rm cm^{-3}}$, illumination factor $G_0 = 10$, and maximum extinction $A_{V,\rm max} = 10$. For the shock component, we run a small set of models with the Paris-Durham shock code,[25] with density $n_{\rm H} = 10\ {\rm cm^{-3}}$, illumination factor $G_0 = 10$, extinction $A_V = 1$, magnetic field strength $b = 0.1$, and velocities from 1–40 $\mathrm{km\ s^{-1}}$ in steps of 5 $\mathrm{km\ s^{-1}}$. The velocity distribution of the shocks is assumed to follow an exponential decay: $f_s\,dv_s \propto (1/\sigma_s)\exp(-v_s/\sigma_s)dv_s$. All of the PDRs are assumed to have the same $G_0 = 10$.

Even with this relatively simple model decomposition, we are nevertheless able to reproduce the observed H_2 intensities quite well, within a reduced $\chi^2 \sim 1.5$. Figure 13 shows the final model decomposition, which reveals that the majority of the H_2 emission is a result of shocks rather than PDRs (note the logarithmic y-axis). On average, ∼88% of each line's emission comes from shocks, with the remaining ∼12% from PDRs. The only line that has a significantly higher PDR contribution is the $S(1)$ line, with ∼35%. We caution that the relative PDR/shock contributions are highly uncertain, because they are primarily informed by a single line ($S(1)$), which itself has a high flux uncertainty. The PDR contributions for the $S(2)$–$S(8)$ lines may lie anywhere from 2%–24%, and the PDR contribution for $S(1)$ is constrained to be $\gtrsim$9%. Despite these limitations, the large shock contributions provide a potential explanation for the enhanced H_2-to-PAH ratios from Figure 10, and are in line with the H_2-to-continuum ratios from Figure 9 if we assume L_{24} is being enhanced by AGN emission. The velocity width for the shock distribution is $\sigma_s \simeq 4\,\mathrm{km\,s^{-1}}$, indicating a contribution primarily from low-velocity shocks.

According to the morphology from Figure 12 and the model decomposition from Figure 13, it appears that the majority of H_2 emission is produced by low-velocity jet-induced shocks in the surrounding medium of the central galaxy. As a sanity check on this interpretation, we now look at the energy budget to confirm the plausibility that the observed level of H_2 emission could be powered by the AGN jets. We calculate the total mechanical power dissipated by a continuous distribution of shocks at different velocities following Equation (6) in J. A. Villa-Vélez et al. (2024):

$$L_{\rm K} = \frac{1}{2}\rho_0\left(\int f_s(v_s)\,v_s^3\,{\rm d}v_s\right)D_A^2 \tag{5}$$

where $\rho_0 = \mu m_p n_{\rm H}$ is the pre-shock density, v_s is the shock velocity, $f_s(v_s)$ is the probability distribution over v_s, and D_A is the angular diameter distance of the source. A mean molecular weight of $\mu \simeq 1.4$ is typical for these types of regions. Using this formula, we obtain $L_{\rm K} \simeq (4\text{–}7) \times 10^{42}\,\mathrm{erg\,s^{-1}}$. The mechanical jet power, on the other hand, has been estimated from the power needed to inflate the large buoyant bubbles to the north and south of the nucleus by M. McDonald et al. (2019). They found a jet power of $L_{\rm jet} \simeq 10^{46}\,\mathrm{erg\,s^{-1}}$. In other words, the mechanical power dissipation from shocks represents only a tiny fraction of the available jet power: $L_{\rm K}/L_{\rm jet} \simeq (0.04\%\text{–}0.07)\%$. This is in line with other analyses, which have found this fraction to not exceed ∼1% (M. Pereira-Santaella et al. 2022).

We can similarly check the total reprocessed UV luminosity that would be required to generate a distribution of PDRs in accordance with the modeled PDR contribution to the H_2 luminosity. Following Equation (8) in J. A. Villa-Vélez et al. (2024):

$$L_{\rm UV} = 1.92 \times 10^{-3}(G_0 + 1)\left(\int f_p(G_0){\rm d}G_0\right)D_A^2 \tag{6}$$

where G_0 is the PDR illumination factor and $f_p(G_0)$ is the probability distribution over G_0 (which, in our case, is just a delta function). From this, we obtain $L_{\rm UV} \simeq (1\text{–}6) \times 10^{45}\,\mathrm{erg\,s^{-1}}$. We can compare this to the reprocessed UV luminosity observed as infrared emission in the SED. The integrated 5–1000 μm luminosity from our CIGALE model, subtracting the AGN component, is $L_{\rm TIR} \simeq 3 \times 10^{46}\,\mathrm{erg\,s^{-1}}$. The observed value is higher by ∼an order of magnitude, which is to be expected when the emission is dominated by shocks. A large fraction of the observed $L_{\rm TIR}$ likely does not originate in reprocessed stellar light, but instead originates from dust that has been heated from shocks and direct radiation from the AGN.

4.1.3. Cooling H_2 from the Hot Atmosphere

In general, the cooling signal in the molecular phase, especially in a system with such a vigorous starburst, will be much weaker than the heating signal from stellar and shock ionization. However, we can analyze the cooling H_2 gas from an energetic and timescale perspective.

The turbulent kinetic energy in the H_2 gas can be estimated from the mass $M_{\rm H_2}$ and velocity dispersion $\sigma_{\rm H_2}$ as

$$E_{\rm H_2} = \frac{3}{2}M_{\rm H_2}\sigma_{\rm H_2}^2 \tag{7}$$

[24] https://ism.obspm.fr/pdr.html
[25] https://ism.obspm.fr/shock.html

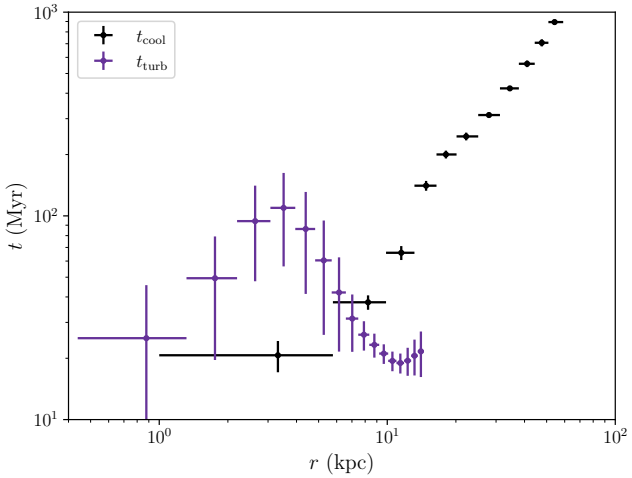

Figure 14. A radial profile of the turbulent dissipation time of the H_2 gas (t_{turb}, in purple) and the cooling time of the hot gas (t_{cool}, in black) in the core region of the cluster. The cooling time profile is taken from M. McDonald et al. (2019). t_{turb} rises above t_{cool} at distances $\lesssim$6–8 kpc, indicating that turbulence may have a significant effect on cooling gas in the core of the BCG.

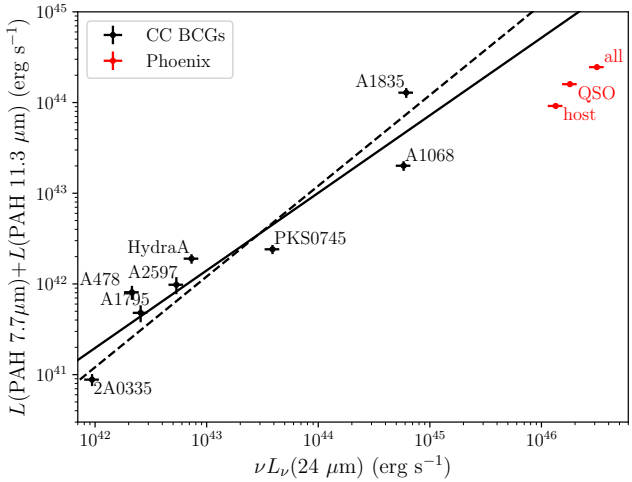

Figure 15. The combined 7.7 μm and 11.3 μm PAH luminosity as a function of the 24 μm continuum luminosity. The ensemble value for Phoenix is plotted against the D11 sample of BCGs. The solid line shows the best-fit power law, and the dashed line shows a slope of 1.

where the factor of 3 comes from converting the observed 1D velocity dispersion to a 3D velocity dispersion ($\sigma = \sqrt{3}\,\sigma_{1D}$). We can use this in conjunction with the observed H_2 luminosity, L_{H_2}, to calculate the expected timescales for the turbulent energy to dissipate:

$$t_{turb} \equiv \frac{E_{H_2}}{L_{H_2}} = \frac{3M_{H_2}\sigma_{H_2}^2}{2L_{H_2}}. \quad (8)$$

We calculate t_{turb} in a series of annuli centered on the point source nucleus, each with a width of 1 pixel (0.″13), extending out to a radius of ∼2.″3 or ∼15 kpc. We compare this to the cooling time of the hot gas, t_{cool}, measured in M. McDonald et al. (2019) in Figure 14.

As σ_{H_2} is based on the line width of the H_2 profile, it represents an upper limit on the amount of turbulence that can be expected. Bulk flows and winds can also contribute to broadening in the observed line profiles through large apertures. Therefore, we interpret the turbulent dissipation timescale as an upper limit. At large radii, $t_{turb} \ll t_{cool}$, such that along the filaments, cooling gas from the hot atmosphere should be unaffected by turbulence. Moving inward, there is a turnover point at around ∼6–8 kpc where the two timescales are comparable. Inward from this point, $t_{turb} \gtrsim t_{cool}$. In this core region, turbulence may have a significant effect on the cooling and condensing of gas into molecular clouds. Primarily, it will prevent the gravitational collapse of cold H_2 clouds into stars, lowering the SFR. Effectively, the actual time for the gas to cool and form stars will be dictated by the maximum of t_{cool} and t_{turb}. However, turbulence also likely plays a key role in enhancing cooling at hotter temperatures by fostering mixing between gas phases. We note that this turnover point lies at the same radius as a cloud of rapidly cooling $10^{5.5}$ K [Ne VI] gas reported in R25, which is believed to be seeded by turbulence and mixing. Taken as a whole, these timescale profiles, combined with the kinematic maps from Figure 3, support a picture in which the H_2 gas forms as a result of cooling along the filaments, flows inward to the core, and a small fraction of it ($\lesssim$1% by mass) is (re)heated to a few 1000 K by turbulent mixing, shock heating, and stellar ionization, in the core region.

4.1.4. PAH Emission

The PAH features are emitted by bending and stretching modes of the bonds between carbon and hydrogen atoms in very small dust grains (A. Leger & J. L. Puget 1984; F. Boulanger et al. 1998; C. Van Kerckhoven et al. 2000)—these modes can be excited by the absorption of UV photons (L. J. Allamandola et al. 1985; G. C. Sloan et al. 1999), making PAH emission a strong tracer of the stellar ionization field (N. M. Förster Schreiber et al. 2004; E. Peeters et al. 2004; B. R. Brandl et al. 2006). Thus, in typical star-forming galaxies where the IR continuum is primarily a result of reprocessed stellar light by larger dust grains, the PAH and continuum luminosity are observed to be strongly correlated with each other (Y. Wu et al. 2010). D11 found that such a correlation also exists in their sample of cool core BCGs, indicating that starlight is still the main contributor to the observed PAH luminosities, even in massive elliptical galaxies. We plot this relationship, recreating D11's Figure 8(a), in Figure 15. Phoenix noticeably falls below the trend seen in the other BCGs, even after subtracting the QSO PSF, by 2.5σ–3σ (where σ here is the scatter in the L_{24}–L_{PAH} relation). This may be due to contamination of the underlying continuum with non-stellar-reprocessed emission, and/or it may be the result of PAH emission being suppressed by the presence of a hard radiation field from an AGN, as has been shown to be the case in numerous studies (P. F. Roche et al. 1991; Y. Xie & L. C. Ho 2022). Such hard radiation can also be emitted from the hot ICM in a cluster environment, leading D11 to conclude that the IR-emitting PAHs seen in BCGs must somehow be shielded from the hot gas, perhaps through a layer of dusty gas with larger dust grains. Additionally, Phoenix's powerful AGN is heavily dust obscured, leading to the potential for localized pockets where PAHs can exist, shielded from both the AGN and the ICM.

We can constrain the ionization source of the PAHs by considering the ratio of the 7.7–11.3 μm PAH features, $L_{7.7}/L_{11.3}$, which is sensitive primarily to the fraction of ionized and neutral PAHs in the system (B. T. Draine &

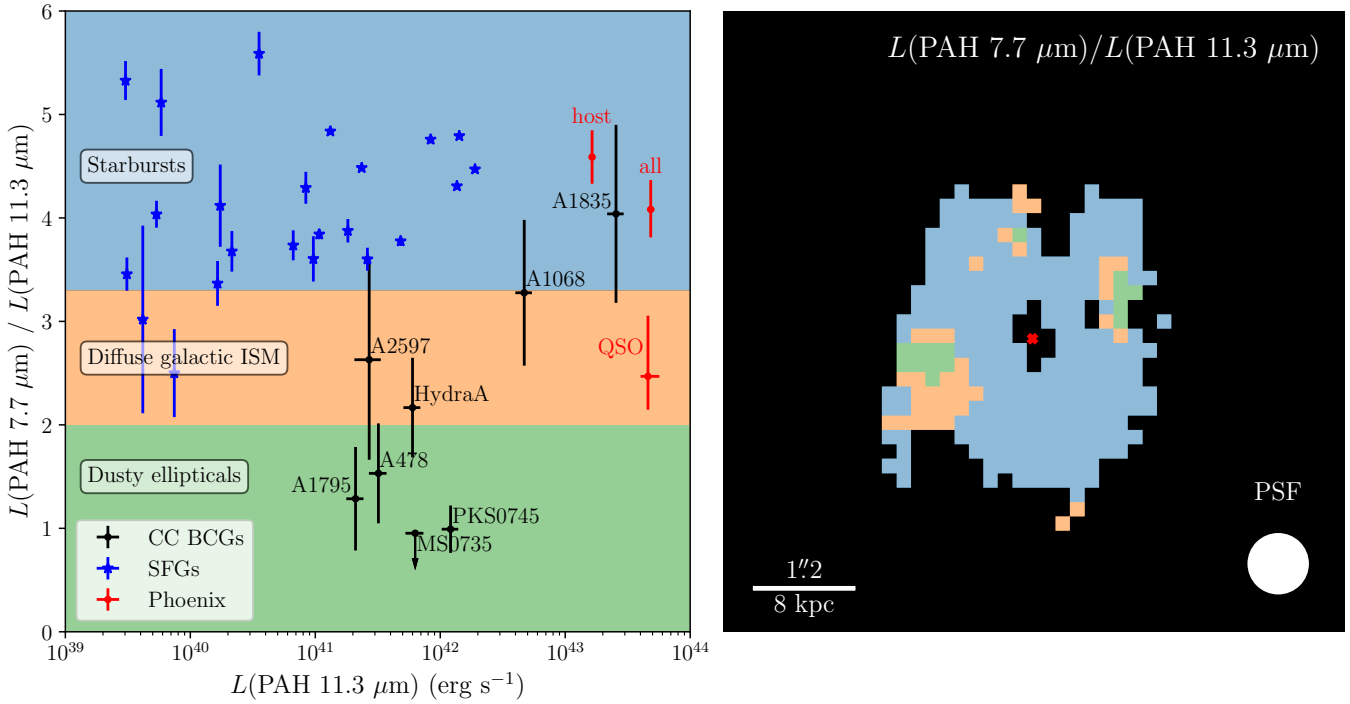

Figure 16. Left panel: the ratio of the 7.7 μm PAH luminosity over the 11.3 μm PAH luminosity as a function of the 11.3 μm PAH luminosity. Different regions are colored according to the dominant ionization mechanisms expected to produce PAH ratios in this regime: starbursts (blue), diffuse galactic ISM (orange), and dusty ellipticals (green). The D11 sample is plotted in black, Phoenix is shown in red, and the SINGS star-forming galaxies are shown in blue. The data points are labeled identically to Figure 9. Right panel: a 2D map of the PAH luminosity ratio in each spaxel. Only spaxels where both PAHs are detected with an S/N $\geqslant 1$ are shown. The spaxels are colored according to which region they fall in on the left panel. A scale bar with physical and angular units is shown in the bottom left, and a circle displaying the size of the PSF FWHM is shown in the bottom right.

A. Li 2007). Starburst systems with a large population of young, hot stars and a hard radiation field typically having elevated ratios of ∼3–7 (J. D. T. Smith et al. 2007). The diffuse galactic ISM, with more evolved stars and an intermediate radiation field, has ratios between 2 and 3.3 (I. Sakon et al. 2004). Finally, dusty elliptical galaxies, with only evolved stars and a soft radiation field, typically have much lower ratios between 1 and 2 (H. Kaneda et al. 2008). We examine $L_{7.7}/L_{11.3}$ in each spaxel and classify them into three categories, for simplicity: "starbursts" (young stars; $L_{7.7}/L_{11.3} > 3.3$), "diffuse galactic ISM" (middle-aged stars; $2 < L_{7.7}/L_{11.3} < 3.3$), and "dusty ellipticals" (old stars; $L_{7.7}/L_{11.3} < 2$). The results are shown in Figure 16. Compared with the D11 sample and the SINGS sample, we see that most of Phoenix A's host galaxy has ratios typical of starburst galaxies. However, there are a few pockets to the southeast and northwest of the nucleus where the ratio drops all the way into dusty elliptical territory. This may indicate that the cooling flow is more suppressed in these regions compared to their surroundings, preventing younger stars from forming and causing the primary ionization source to be old stars. Alternatively, these regions may have a higher dust obscuration around the young stars, but we do not see any coincidence between the pockets of low PAH ratios here and regions of enhanced dust obscuration in Figure 2.

The ratio also drops significantly in the nucleus (as shown by the "QSO" data point), following the trends seen in J. D. T. Smith et al. (2007) for AGN-dominated systems. The hard ionizing radiation from an AGN is thought to have a profound effect on PAHs, changing both their grain size distribution and ionization fraction. Ionized PAHs are preferentially destroyed relative to neutral PAHs, leading to lowered $L_{7.7}/L_{11.3}$ ratios. Recent JWST results from the GATOS collaboration (I. García-Bernete et al. 2024) suggest that AGN radiation can have noticeable effects on the PAH ionization fraction even at kiloparsec scales, particularly in regions showing signs of jet or outflow activity from the AGN. This may provide an alternate explanation for the pockets of lowered $L_{7.7}/L_{11.3}$ ratios to the east and west of the nucleus, although these do not lie along the jet axis of the AGN in this system. There is also an indirect effect on the PAH ratios caused by the suppression of star formation within the inner ∼1 kpc from the SMBH—at this scale, the closer to the SMBH, the more effective heating becomes. This has been observed in simulations with substantial rises in the innermost entropy and turbulence (e.g., D. Wittor & M. Gaspari 2020).

4.1.5. Star Formation Rates

The literature has many calibrated SFR correlations with host galaxy properties, including integrated continuum luminosities, single-band continuum luminosities, and emission-line luminosities. These correlations are applicable only in certain circumstances, so they can be compared and taken advantage of to infer whether these conditions hold. Here, we analyze SFRs from a number of different indicators in comparison to our modeled SFR from the SED (Section 3.2), which we take to be the "true" (read: most accurate) value.

First, the SFR can be estimated from the total infrared luminosity $L_{\rm TIR}$ (integrated from 5–1000 μm) using R. C. J. Kennicutt (1998), and the 70 μm luminosity $L_{70} \equiv \nu L_\nu(70\ \mu\text{m})$ using D. Calzetti et al. (2010). We recreate D11's Figure 4 in Figure 17, showing both of these correlations for Phoenix, using $L_{\rm TIR}$ and L_{70} obtained from

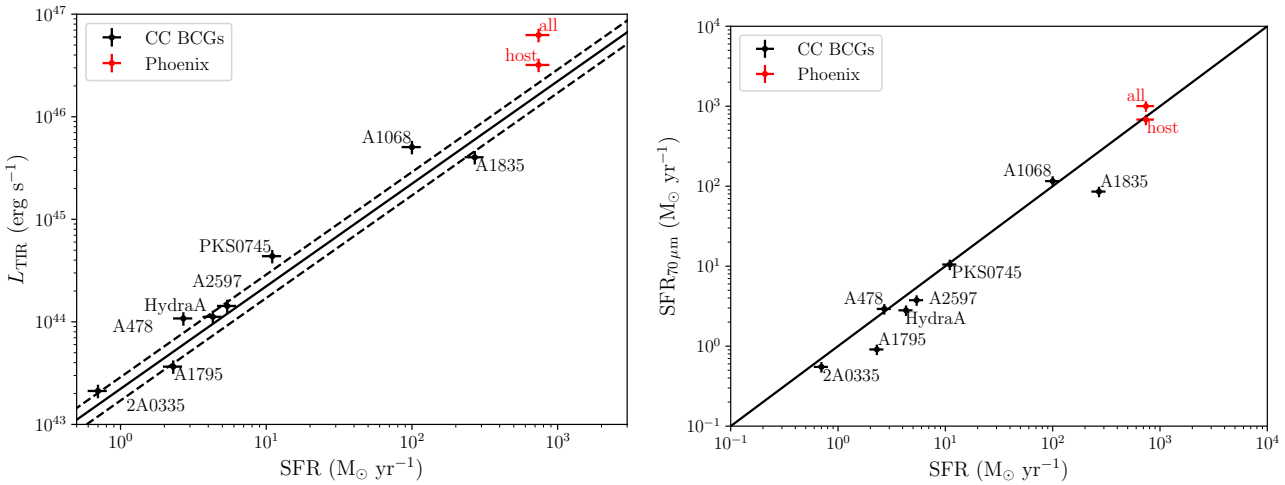

Figure 17. Left panel: the total infrared luminosity $L_{\rm TIR}$ integrated from 5–1000 μm, as a function of the modeled SFR. The solid line shows the R. C. J. Kennicutt (1998) relation, and the dashed lines show a 30% scatter on that relation. Right panel: the SFR estimated from the monochromatic 70 μm luminosity as a function of the modeled SFR. The solid line shows the D. Calzetti et al. (2010) relation.

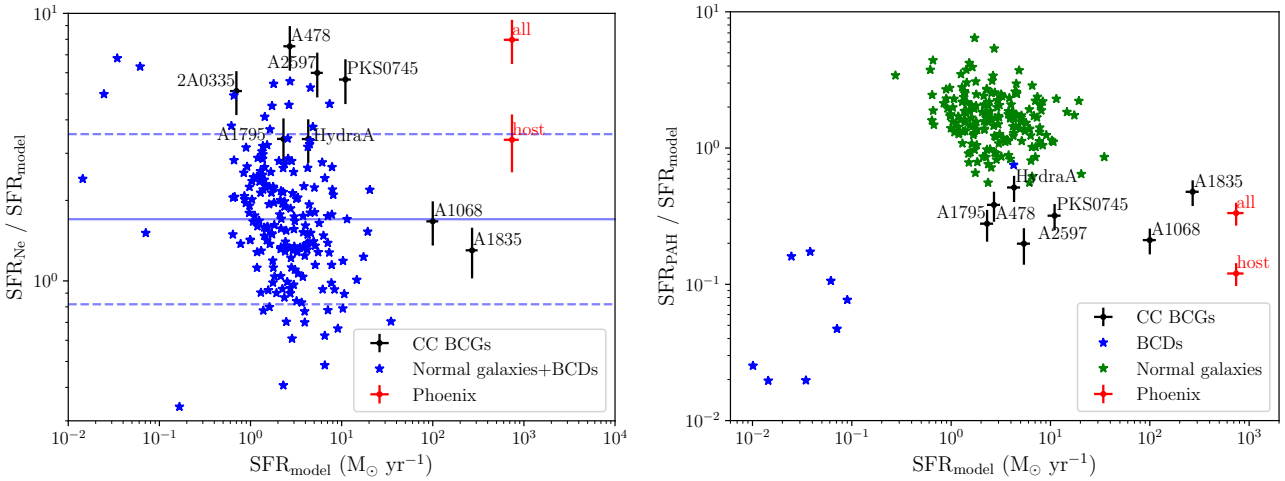

Figure 18. Left panel: a comparison between the SFR estimated from the [Ne II] and [Ne III] line luminosities and the SFR modeled from the SED. The data points for the BCGs are in black, Phoenix is in red, and Y. Xie & L. C. Ho (2019) galaxies are in blue. For Y. Xie & L. C. Ho (2019) galaxies, "SFR$_{\rm model}$" refers to SFRs from the MPA/JHU catalog. The solid blue line shows the average value of the Y. Xie & L. C. Ho (2019) galaxies, while the dashed blue line shows the 1σ standard deviation. Right panel: a comparison between the SFR estimated from the 7.7 μm and 11.3 μm PAH luminosities and the SFR estimated from SED modeling. The colors here are the same, except that the Y. Xie & L. C. Ho (2019) galaxies are split up into blue compact dwarfs (BCDs; in blue) and non-BCDs (in green). The BCDs here do not use the different scaling relation parameters for galaxies with $M_* < 10^9\,M_\odot$ as suggested by Y. Xie & L. C. Ho (2019), to highlight the apparent deficit in PAHs in these systems.

the SED fitting. We notice that the $L_{\rm TIR}$ correlation in particular would vastly overpredict the SFR at $>2000\,M_\odot\,{\rm yr}^{-1}$ if no AGN correction is accounted for. However, it lines up fairly well after subtracting the AGN contribution. These discrepancies confirm, as we saw in the SED modeling, that the AGN, despite being heavily obscured in the optical, accounts for a significant fraction of the underlying continuum luminosity throughout the whole infrared range. This includes contributions directly from the accretion disk itself, those that get absorbed and re-emitted by dust in the torus and the polar regions, and synchrotron emission (at longer wavelengths) from the bipolar radio jets.

The SFR can also be measured from the [Ne II] and [Ne III] lines (L. C. Ho & E. Keto 2007). Following D11, we take $\rm Ne^+/Ne = 0.75$ and $\rm Ne^{2+}/Ne = 0.15$. We recreate their Figure 12 in Figure 18 (left panel). We include the sample of star-forming galaxies used by Y. Xie & L. C. Ho (2019) as a reference point—for these galaxies, "SFR$_{\rm model}$" refers to SFRs obtained from the MPA/JHU catalog.[26] After subtracting the contribution to the [Ne II] and [Ne III] lines from AGN photoionization, we see that the "host" point lies close to the expected value for SFGs (solid line), but is still marginally enhanced, lying closer to the $+1\sigma$ line (dashed blue line). This may be due to enhanced emission from shocks, as we have seen that the H_2 emission in this system is primarily emitted by shocks (Figure 13), and the H_2 and [Ne II] emission are correlated (Figure 11). Unfortunately, we cannot compare with the H_2-calibrated SFR since it relies on the $S(0)$ line, which falls outside of the wavelength coverage of MIRI at Phoenix's redshift. But considering the strong correlation between the H_2 and [Ne II] luminosities, we can infer that we would likely see good agreement with the modeled SFR value here as well.

Additionally, we can look at the SFR inferred from the PAH features, using the relation calibrated by Y. Xie & L. C. Ho

[26] https://wwwmpa.mpa-garching.mpg.de/SDSS/DR7/

(2019). For each BCG, we take an average of the SFRs inferred from the 7.7 μm and 11.3 μm PAH features. Comparing these SFRs to the modeled values in Figure 18 (right) shows a systematic deficit, with the PAH-based SFRs being 40%–80% lower. In this panel, we also show the Y. Xie & L. C. Ho (2019) sample of galaxies, but now split up between blue compact dwarfs (BCDs) in blue and normal galaxies in green. The normal galaxies have a typical PAH-based SFR in agreement with the modeled SFR. However, we see a decline in both the BCDs and BCGs. Y. Xie & L. C. Ho (2019) addressed this for the BCD population by adopting a different scaling offset for galaxies with $M_* < 10^9\,M_\odot$—we have not included this correction in Figure 18 to highlight the apparent PAH deficit in these galaxies and to show the similarities they have with the BCGs. Phoenix, in particular, has a PAH-based SFR almost an order of magnitude smaller than its modeled value. This may be evidence for a PAH deficit in the high-mass galaxy population similar to the deficit in the BCDs: the Y. Xie & L. C. Ho (2019) relation we utilize is calibrated for the general galaxy population with stellar masses between 10^9 and $10^{11.4}\,M_\odot$, whereas the BCGs we examine here all have stellar masses $\gtrsim 10^{11}\,M_\odot$. This is reinforced by the results of our CIGALE SED models, in which the PAH mass fraction parameter ($q_{\rm PAH}$) is driven to the lowest possible value of 0.47%, an order of magnitude lower than a typical Milky Way–like galaxy with $\sim$4.6% (B. T. Draine & A. Li 2007). The cluster environment may have a significant effect on the survivability of PAHs: collisions with high-energy electrons from the ICM (and an AGN, if active) can sputter and destroy the dust grains on extremely short timescales. D11 argued, using the analysis of E. R. Micelotta et al. (2010), that PAHs embedded in a 1 keV, 0.1 $\rm cm^{-3}$ plasma could not survive longer than a few hundred years. However, dust can also locally enhance cooling, nurturing the formation of cold gas clouds around the dust that act as a protective shield against the energetic electrons and ions in the ICM, allowing the dust to survive longer in these localized cooling regions. E. R. Micelotta et al. (2010) estimated that for conditions similar to the Orion nebula (7000 K, 10^4 $\rm cm^{-3}$), the PAH survivability is much higher, at roughly 10 Myr. The feeding and feedback cycle of the AGN may also play an important role in periodically refreshing the dust content of the ICM by blowing out dust from the nucleus during outbursts and allowing for more dust formation (or, rather, lessened dust sputtering) during periods of inactivity.

4.2. An Undermassive Black Hole?

With the SFRs of order $\sim$1000 $M_\odot\,\rm yr^{-1}$ and molecular gas masses of order $\sim 10^{10}\,M_\odot$ pointing to massive amounts of cooling gas in the Phoenix cluster, the question then becomes: what makes this cluster unique? Why is this cluster able to host a massive cooling flow while every other observed cluster cannot? The simplest explanation is that there is nothing particularly special about the Phoenix cluster, but we just happened to be observing it at a time when it is undergoing a short-lived cooling spike that will not last much longer than $\sim$a few Myr (as we proposed in R25). This scenario is supported by simulations at both the cluster scale (M. Gaspari et al. 2017) and black hole scale (R. S. Beckmann et al. 2019), which predict that feeding and feedback follow an episodic cycle. If indeed all clusters undergo a phase of rapid cooling once throughout their lifetimes, then we should expect to see about 1 in every 10,000 clusters (which is roughly the amount of clusters known—e.g., M. Klein et al. 2024) experiencing such an event. This seems to line up with expectations, but it becomes problematic when we consider that clusters should still exhibit post-starburst signatures long after they have experienced these rapid cooling spikes. These features are generally not seen, even in cool core clusters, and are more often associated with other processes such as galaxy interactions, mergers, and ram pressure stripping (A. Werle et al. 2022). Therefore, it seems that we can rule out the presupposition that there is nothing special at all about the Phoenix cluster.

Another idea, previously explored in M. McDonald et al. (2018) and M. McDonald et al. (2019), is that the Phoenix cluster hosts an undermassive SMBH relative to the size of its cool core, which is expected to occur in the most-massive galaxy clusters. In this scenario, rapid cooling drives the accretion rate of the AGN to high Eddington ratios ($\dot{M}/\dot{M}_{\rm Edd} \lesssim 5\%$). But at these higher Eddington ratios, much of the power output of the AGN comes in the form of radiative feedback as opposed to mechanical feedback, which is less effective at suppressing cooling and may even enhance it through the inverse Compton effect close to the AGN (M. McDonald et al. 2019). Indeed, H. R. Russell et al. (2013) showed that mechanical power output tends to become saturated at $\sim$1% of the Eddington luminosity, while radiative power continues to grow with the accretion rate.

While there are currently only weak constraints on the mass of Phoenix's black hole, it is confirmed to show signs of both radiative (bright SEDs; Section 3.2; M. McDonald et al. 2012) and mechanical (X-ray cavities, radio jets; J. Hlavacek-Larrondo et al. 2015; R. Timmerman et al. 2021) feedback. Estimates of the mechanical power output place it at $0.5\text{–}1 \times 10^{46}\,\rm erg\,s^{-1}$ (M. McDonald et al. 2019), while we can estimate from our SED fitting in Section 3.2 a radiative power output of $L_{\rm bol} = 3 \times 10^{46}\,\rm erg\,s^{-1}$. The fact that these are similar in magnitude suggests that the AGN has only recently undergone (or perhaps is still undergoing) a transition in feedback modes (M. McDonald et al. 2015). In addition, the mechanical power is just high enough to balance with the cooling luminosity of $\sim 10^{46}\,\rm erg\,s^{-1}$ (M. McDonald et al. 2019), and it corresponds to the mechanical feedback limit of a $\sim 10^{10}\,M_\odot$ black hole. If Phoenix's black hole has only recently experienced a period of rapid growth up to $10^{10}\,M_\odot$, this would explain the puzzlingly high rates of cooling despite the black hole's current power output being seemingly large enough that it should offset this cooling.

As the cluster continues to evolve, in this picture, we should expect the cooling to begin being regulated more efficiently by the recently grown black hole. Now that the mechanical power output has reached levels sufficient to balance cooling, the cooling rates, SFRs, and accretion rate of the SMBH should all slow down until they reach roughly the percent level of the classical cooling rate. In fact, we can estimate from the bolometric AGN luminosity that the black hole's current accretion rate is $\dot{M} = L_{\rm bol}/\eta c^2 \approx 5\,M_\odot\,\rm yr^{-1}$ (assuming an efficiency $\eta = 0.1$), which is about an order of magnitude lower than previously thought (due to uncertain X-ray-to-bolometric luminosity corrections; M. McDonald et al. 2012). This may indeed be an indication that the black hole's growth has now slowed after reaching a mass sufficient to balance cooling. This trend will ultimately drive Phoenix toward

A1835 and A1068 on many of our figures, decreasing dramatically in L_{24} as the AGN radiative power output diminishes, and decreasing less dramatically in other quantities (L_{H_2}, $L_{[NeII]}$, L_{PAH}). The ratio of the 7.7–11.3 μm PAH features will also decrease with the SFR, trending toward values more typical of the diffuse galactic ISM. The PAH-derived SFRs, however, will likely stay suppressed relative to other SFR indicators, as this seems to be largely due to the influence of the ICM and is not a feature specific to Phoenix. Whether this scenario holds up in reality would largely be determined with more precise constraints on the SMBH mass.

5. Conclusion

Since its discovery, the Phoenix Cluster has stood out as a unique system, even among cool core clusters, due to its hosting of the most-massive and efficient cooling flow in the known Universe (M. McDonald et al. 2012). The results of our analysis of the molecular gas, dust, and star formation from MIRI/MRS data have only further exemplified this uniqueness. We list the important results of our analysis, in sequence, below:

1. We have measured the optical depth due to silicate absorption in the warm molecular line-emitting gas based on fitting excitation models of the rotational H_2 lines, finding that the silicate dust traces cooling regions and has a similar morphology to other types of dust.
2. Using this technique in conjunction with the LOKI spectral modeling software, we have measured the total molecular gas mass in the Phoenix cluster to be $1.9^{+0.5}_{-0.4} \times 10^{10}\,M_\odot$, in agreement with previous estimates made using CO emission. We have estimated the CO-to-H_2 conversion factor to be $\alpha_{CO} = 0.8 \pm 0.2 M_\odot\,\mathrm{pc}^{-2}\,(\mathrm{K\,km\,s}^{-1})^{-1}$.
3. We have filled in the MIR gap in Phoenix's SED and obtained refined measurements of the stellar mass, $M_* = 2.6 \pm 0.5 \times 10^{12}\,M_\odot$, and SFRs, $\langle \mathrm{SFR} \rangle_{10} = 1340 \pm 100\,M_\odot\,\mathrm{yr}^{-1}$ and $\langle \mathrm{SFR} \rangle_{100} = 740 \pm 80\,M_\odot\,\mathrm{yr}^{-1}$, in agreement within $\pm 1\sigma$ of previous estimates based on a number of different scaling relations (M. McDonald et al. 2012).
4. We have developed a complete picture to explain the observed H_2 emission in the Phoenix cluster, motivated by a comprehensive analysis of the kinematics, energetics, and morphology. The hot atmosphere cools and condenses along the filaments at distances $\gtrsim$8 kpc, before flowing inward toward the core. In the core region $\lesssim$8 kpc, the molecular gas encounters turbulence from the AGN's radio jets and stellar feedback, which slows down the cooling process by ∼an order of magnitude. The molecular gas is (re)heated by stellar radiation, shocks, and potentially by mixing with hotter gas phases, all of which also contribute toward enhancing the H_2 luminosity per unit mass, decreasing α_{CO}.
5. We have uncovered an apparent PAH deficit in the $\gtrsim 10^{11}\,M_\odot$ cool core BCG population, causing their PAH-based SFRs to be underpredicted by up to an order of magnitude. This is distinct from the deficit found in galaxies with a strong AGN, like Phoenix, as the other BCGs in the sample all show little to no signs of AGN activity. This may be a result of suprathermal ICM particle heating, creating a harsh environment unsuitable for the sustained existence of PAH grains.
6. We have updated the measurement of the bolometric luminosity of Phoenix's AGN, finding $L_{bol} = 3 \times 10^{46}\,\mathrm{erg\,s}^{-1}$, an order of magnitude lower than previous estimates based on an X-ray-to-bolometric correction (M. McDonald et al. 2012). The fact that this is comparable to the mechanical power output from the jets ($L_{jet} \simeq 10^{46}\,\mathrm{erg\,s}^{-1}$) suggests a transition in feedback modes is currently underway and lends credence to the theory that Phoenix hosts an undermassive central black hole relative to the size of its halo.

Taken together, our analyses provide even more evidence to suggest that the Phoenix cluster is experiencing a highly efficient, but still turbulent and chaotic, top-down cascade of condensation and cooling from the hot ICM down to the cold molecular phase. We are seeing the effects of this cooling propagate through the young stellar populations, and then feeding back into the gas, dust, and PAHs through the interstellar radiation field, shocks, and turbulence.

Acknowledgments

This work is based on observations with the NASA/ESA/CSA James Webb Space Telescope obtained from the Data Archive at the Space Telescope Science Institute, which is operated by the Association of Universities for Research in Astronomy, Incorporated, under NASA contract NAS 5-03127. Support for program No. JWST-GO-02439.001-A was provided through a grant from the STScI under NASA contract NAS 5-03127. M.R. acknowledges support from the National Science Foundation Graduate Research Fellowship under grant No. 2141064. M.Chatzikos acknowledges support from NASA (19-ATP19-0188, 22-ADAP22-0139) and NSF (1910687). M.G. acknowledges support from the ERC Consolidator Grant BlackHoleWeather (101086804). H.R.R. acknowledges an Anne McLaren Fellowship from the University of Nottingham.

Facility: JWST.

Software: `julia` (J. Bezanson et al. 2017), `LOKI.jl` (M. Reefe 2025, https://github.com/Michael-Reefe/Loki.jl), `python` (G. Van Rossum & F. L. Drake 2009), `numpy` (C. R. Harris et al. 2020), `scipy` (P. Virtanen et al. 2020), `astropy` (Astropy Collaboration et al. 2013), `matplotlib` (J. D. Hunter 2007), `SAOImage DS 9` (Smithsonian Astrophysical Observatory 2000).

All JWST data used in this paper can be found in MAST: doi:10.17909/pc04-3145. Note that 24 μm fluxes for the D. Farrah et al. (2007) sample were obtained with NED (NASA/IPAC Extragalactic Database NED).

ORCID iDs

Michael Reefe https://orcid.org/0000-0003-4701-8497
Michael McDonald https://orcid.org/0000-0001-5226-8349
Marios Chatzikos https://orcid.org/0000-0002-8823-0606
Richard Mushotzky https://orcid.org/0000-0002-7962-5446
Sylvain Veilleux https://orcid.org/0000-0002-3158-6820
Steven W. Allen https://orcid.org/0000-0003-0667-5941
Matthew Bayliss https://orcid.org/0000-0003-1074-4807
Michael Calzadilla https://orcid.org/0000-0002-2238-2105
Rebecca Canning https://orcid.org/0000-0003-1398-5542
Megan Donahue https://orcid.org/0000-0002-2808-0853

Benjamin Floyd https://orcid.org/0000-0003-4175-571X
Massimo Gaspari https://orcid.org/0000-0003-2754-9258
Julie Hlavacek-Larrondo https://orcid.org/0000-0001-7271-7340
Brian McNamara https://orcid.org/0000-0002-2622-2627
Helen Russell https://orcid.org/0000-0001-5208-649X
Arnab Sarkar https://orcid.org/0000-0002-5222-1337
Keren Sharon https://orcid.org/0000-0002-7559-0864
Taweewat Somboonpanyakul https://orcid.org/0000-0003-3521-3631

References

Allamandola, L. J., Tielens, A. G. G. M., & Barker, J. R. 1985, ApJL, 290, L25
Allen, S. W. 1995, MNRAS, 276, 947
Astropy Collaboration, Robitaille, T. P., Tollerud, E. J., et al. 2013, A&A, 558, A33
Beckmann, R. S., Devriendt, J., & Slyz, A. 2019, MNRAS, 483, 3488
Bezanson, J., Edelman, A., Karpinski, S., & Shah, V. B. 2017, SIAMR, 59, 65
Bicknell, G. V., Sutherland, R. S., van Breugel, W. J. M., et al. 2000, ApJ, 540, 678
Bolatto, A. D., Wolfire, M., & Leroy, A. K. 2013, ARA&A, 51, 207
Boquien, M., Burgarella, D., Roehlly, Y., et al. 2019, A&A, 622, A103
Bordoloi, R., Wagner, A. Y., Heckman, T. M., & Norman, C. A. 2017, ApJ, 848, 122
Boulanger, F., Boisssel, P., Cesarsky, D., & Ryter, C. 1998, A&A, 339, 194
Brandl, B. R., Bernard-Salas, J., Spoon, H. W. W., et al. 2006, ApJ, 653, 1129
Calura, F., Pipino, A., & Matteucci, F. 2008, A&A, 479, 669
Calzadilla, M. S., Bleem, L. E., McDonald, M., et al. 2023, ApJ, 947, 44
Calzetti, D., Wu, S. Y., Hong, S., et al. 2010, ApJ, 714, 1256
Canizares, C. R., Markert, T. H., & Donahue, M. E. 1988, in Proc. NATO Advanced Study Institute (ASI) Series C, Vol. 229, Cooling Flows in Clusters and Galaxies, ed. A. C. Fabian (Dordrecht: Kluwer), 63
Crawford, C. S., Allen, S. W., Ebeling, H., Edge, A. C., & Fabian, A. C. 1999, MNRAS, 306, 857
Dale, D. A., Gil de Paz, A., Gordon, K. D., et al. 2007, ApJ, 655, 863
David, L. P., Nulsen, P. E. J., McNamara, B. R., et al. 2001, ApJ, 557, 546
Donahue, M., Connor, T., Fogarty, K., et al. 2015, ApJ, 805, 177
Donahue, M., de Messières, G. E., O'Connell, R. W., et al. 2011, ApJ, 732, 40
Downes, D., & Solomon, P. M. 1998, ApJ, 507, 615
Downes, D., Solomon, P. M., & Radford, S. J. E. 1993, ApJL, 414, L13
Draine, B. T., & Li, A. 2007, ApJ, 657, 810
Edge, A. C. 2001, MNRAS, 328, 762
Edwards, L. O. V., Hudson, M. J., Balogh, M. L., & Smith, R. J. 2007, MNRAS, 379, 100
Fabian, A. C. 2012, ARA&A, 50, 455
Fabian, A. C., Ferland, G. J., Sanders, J. S., et al. 2022, MNRAS, 515, 3336
Fabian, A. C., Nulsen, P. E. J., & Canizares, C. R. 1984, Natur, 310, 733
Fabian, A. C., Sanders, J. S., Ferland, G. J., et al. 2023, MNRAS, 521, 1794
Farrah, D., Bernard-Salas, J., Spoon, H. W. W., et al. 2007, ApJ, 667, 149
Förster Schreiber, N. M., Roussel, H., Sauvage, M., & Charmandaris, V. 2004, A&A, 419, 501
García-Bernete, I., Rigopoulou, D., Donnan, F. R., et al. 2024, A&A, 691, A162
Gaspari, M., McDonald, M., Hamer, S. L., et al. 2018, ApJ, 854, 167
Gaspari, M., Melioli, C., Brighenti, F., & D'Ercole, A. 2011, MNRAS, 411, 349
Gaspari, M., Temi, P., & Brighenti, F. 2017, MNRAS, 466, 677
Gaspari, M., Tombesi, F., & Cappi, M. 2020, NatAs, 4, 10
Harris, C. R., Millman, K. J., van der Walt, S. J., et al. 2020, Natur, 585, 357
Hatch, N. A., Crawford, C. S., & Fabian, A. C. 2007, MNRAS, 380, 33
Hicks, A. K., & Mushotzky, R. 2005, ApJL, 635, L9
Hlavacek-Larrondo, J., McDonald, M., Benson, B. A., et al. 2015, ApJ, 805, 35
Ho, L. C., & Keto, E. 2007, ApJ, 658, 314
Hoffer, A. S., Donahue, M., Hicks, A., & Barthelemy, R. S. 2012, ApJS, 199, 23
Hunter, J. D. 2007, CSE, 9, 90
Kaneda, H., Onaka, T., Sakon, I., et al. 2008, ApJ, 684, 270
Kaviraj, S., Ting, Y.-S., Bureau, M., et al. 2012, MNRAS, 423, 49
Kennicutt, R. C. J. 1990, in Astrophysics and Space Science Library, The Interstellar Medium in Galaxies, Vol. 161, ed. J. Thronson, A. Harley, & J. M. Shull (Dordrecht: Kluwer), 405
Kennicutt, R. C. J. 1998, ARA&A, 36, 189
Klein, M., Mohr, J. J., & Davies, C. T. 2024, A&A, 690, A322
Labiano, A., Argyriou, I., Álvarez-Márquez, J., et al. 2021, A&A, 656, A57
Le Petit, F., Nehmé, C., Le Bourlot, J., & Roueff, E. 2006, ApJS, 164, 506
Leger, A., & Puget, J. L. 1984, A&A, 137, L5
Li, Y., Ruszkowski, M., & Bryan, G. L. 2017, ApJ, 847, 106
Madau, P., & Dickinson, M. 2014, ARA&A, 52, 415
McDonald, M., Bayliss, M., Benson, B. A., et al. 2012, Natur, 488, 349
McDonald, M., Benson, B., Veilleux, S., Bautz, M. W., & Reichardt, C. L. 2013, ApJL, 765, L37
McDonald, M., Gaspari, M., McNamara, B. R., & Tremblay, G. R. 2018, ApJ, 858, 45
McDonald, M., McNamara, B. R., van Weeren, R. J., et al. 2015, ApJ, 811, 111
McDonald, M., McNamara, B. R., Voit, G. M., et al. 2019, ApJ, 885, 63
McDonald, M., Swinbank, M., Edge, A. C., et al. 2014, ApJ, 784, 18
McDonald, M., Veilleux, S., Rupke, D. S. N., & Mushotzky, R. 2010, ApJ, 721, 1262
McNamara, B. R., & Nulsen, P. E. J. 2007, ARA&A, 45, 117
McNamara, B. R., & O'Connell, R. W. 1989, AJ, 98, 2018
Micelotta, E. R., Jones, A. P., & Tielens, A. G. G. M. 2010, A&A, 510, A37
Mittal, R., Whelan, J. T., & Combes, F. 2015, MNRAS, 450, 2564
Mo, H., van den Bosch, F. C., & White, S. 2010, Galaxy Formation and Evolution (Cambridge: Cambridge Univ. Press)
Molendi, S., Tozzi, P., Gaspari, M., et al. 2016, A&A, 595, A123
NASA/IPAC Extragalactic Database (NED) 2019, NASA/IPAC Extragalactic Database (NED), NASA/IPAC, doi:10.26132/NED1
O'Dea, C. P., Baum, S. A., Privon, G., et al. 2008, ApJ, 681, 1035
Ogle, P., Boulanger, F., Guillard, P., et al. 2010, ApJ, 724, 1193
Peeters, E., Spoon, H. W. W., & Tielens, A. G. G. M. 2004, ApJ, 613, 986
Pereira-Santaella, M., Álvarez-Márquez, J., García-Bernete, I., et al. 2022, A&A, 665, L11
Peterson, J. R., Kahn, S. M., Paerels, F. B. S., et al. 2003, ApJ, 590, 207
Prasad, D., Sharma, P., & Babul, A. 2015, ApJ, 811, 108
Rawle, T. D., Edge, A. C., Egami, E., et al. 2012, ApJ, 747, 29
Reefe, M. 2025, LOKI: Likelihood Optimization of gas Kinematics in IFUs, v2.0, Zenodo, doi:10.5281/zenodo.15069243
Reefe, M., McDonald, M., Chatzikos, M., et al. 2025, Natur, 638, 360
Roche, P. F., Aitken, D. K., Smith, C. H., & Ward, M. J. 1991, MNRAS, 248, 606
Rosenthal, D., Bertoldi, F., & Drapatz, S. 2000, A&A, 356, 705
Roussel, H., Helou, G., Hollenbach, D. J., et al. 2007, ApJ, 669, 959
Russell, H. R., McDonald, M., McNamara, B. R., et al. 2017, ApJ, 836, 130
Russell, H. R., McNamara, B. R., Edge, A. C., et al. 2013, MNRAS, 432, 530
Sakon, I., Onaka, T., Ishihara, D., et al. 2004, ApJ, 609, 203
Salomé, P., & Combes, F. 2003, A&A, 412, 657
Salomé, P., Revaz, Y., Combes, F., et al. 2008, A&A, 483, 793
Sloan, G. C., Hayward, T. L., Allamandola, L. J., et al. 1999, ApJL, 513, L65
Smith, J. D. T., Draine, B. T., Dale, D. A., et al. 2007, ApJ, 656, 770
Smithsonian Astrophysical Observatory, 2000, SAOImage DS 9: A Utility for Displaying Astronomical Images in the X11 Window Environment, Astrophysics Source Code Library, ascl:0003.002
Spilker, J. S., Phadke, K. A., Aravena, M., et al. 2023, Natur, 618, 708
Sutherland, R. S., & Dopita, M. A. 1993, ApJS, 88, 253
Timmerman, R., van Weeren, R. J., McDonald, M., et al. 2021, A&A, 646, A38
Togi, A., & Smith, J. D. T. 2016, ApJ, 830, 18
Treyer, M., Schiminovich, D., Johnson, B. D., et al. 2010, ApJ, 719, 1191
Tychoniec, Ł., van Gelder, M. L., van Dishoeck, E. F., et al. 2024, A&A, 687, A36
Van De Putte, D., Meshaka, R., Trahin, B., et al. 2024, A&A, 687, A86
Van Kerckhoven, C., Hony, S., Peeters, E., et al. 2000, A&A, 357, 1013
Van Rossum, G., & Drake, F. L. 2009, Python 3 Reference Manual (Scotts Valley, CA: CreateSpace)
Veilleux, S., Rupke, D. S. N., Kim, D. C., et al. 2009, ApJS, 182, 628
Viaene, S., Nersesian, A., Fritz, J., et al. 2020, A&A, 638, A150
Villa-Vélez, J. A., Godard, B., Guillard, P., & Pineau des Forêts, G. 2024, A&A, 688, A96
Virtanen, P., Gommers, R., Oliphant, T. E., et al. 2020, NatMe, 17, 261
Werle, A., Poggianti, B., Moretti, A., et al. 2022, ApJ, 930, 43
Williamson, R., Benson, B. A., High, F. W., et al. 2011, ApJ, 738, 139
Wittor, D., & Gaspari, M. 2020, MNRAS, 498, 4983
Wu, Y., Helou, G., Armus, L., et al. 2010, ApJ, 723, 895
Xie, Y., & Ho, L. C. 2019, ApJ, 884, 136
Xie, Y., & Ho, L. C. 2022, ApJ, 925, 218
Yang, G., Boquien, M., Buat, V., et al. 2020, MNRAS, 491, 740